A Sponsored Supplement to *Science*

Optimizing your live-cell microscopy: Tricks and trade-offs

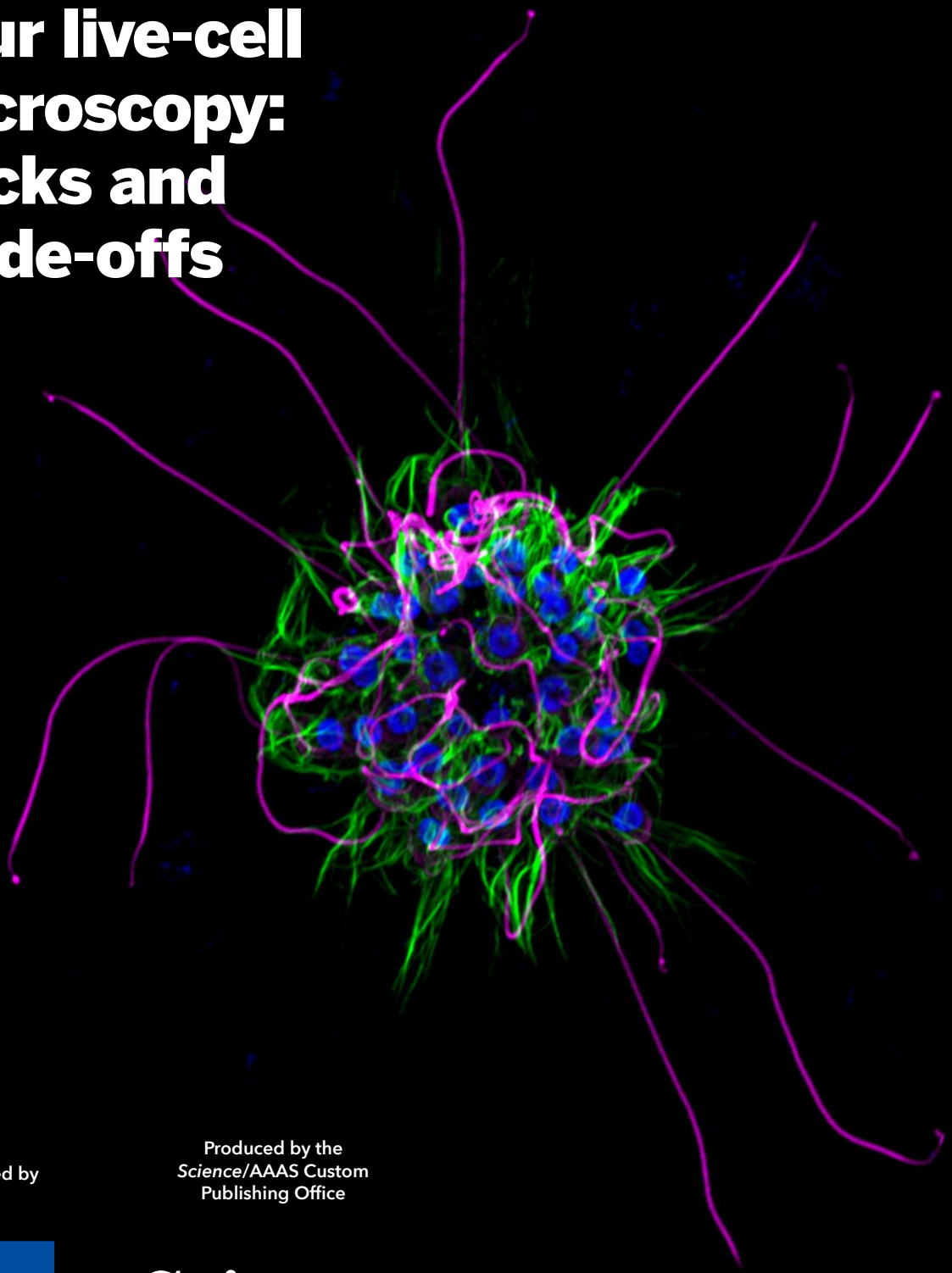

Sponsored by

ZEISS

Produced by the *Science*/AAAS Custom Publishing Office

Science
AAAS

Optimizing your live-cell microscopy: Tricks and trade-offs

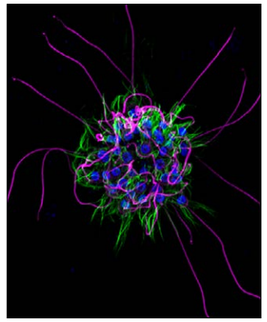

ABOUT THE COVER:
Choanoflagellate rosette colony isolated from Mono Lake, California, stained for DNA, microtubules, and F-actin. Acquired using a ZEISS LSM 880 with Airyscan. Credit: Kayley Hake, University of California, Berkeley.

This booklet was produced by the *Science*/AAAS Custom Publishing Office and sponsored by Carl Zeiss Microscopy GmbH.

Editor: Sean Sanders, Ph.D.
Proofreader/Copyeditor: Bob French
Designer: Amy Hardcastle

BILL MORAN, GLOBAL DIRECTOR
Custom Publishing
bmoran@aaas.org
+1-202-326-6438

ROGER GONCALVES, SALES MANAGER
Custom Publishing
Europe, Middle East, and India
rgoncalves@science-int.co.uk
+41-43-243-1358

A life well lived in the age of microscopy

In the world of cellular biology, the microscope is king. If you want to know what's going on at a cellular or subcellular level, one of the few direct ways of doing so is with some flavor of microscopy. From its invention in the early 1600s (the origin of the first light microscope is somewhat in dispute), inventors and researchers have been constantly improving on the original design through hardware and software upgrades, pushing the boundaries of resolution, speed, and depth of imaging. Seldom does a year pass without a significant advance in this field, most especially in the realm of fluorescent microscopy (which garnered a Nobel Prize in Chemistry in 2014).

For the vast majority of the time since the invention of the microscope, in order to view a specimen, it has needed to be prepared through a permanent fixation procedure. Also, samples are often specially treated to reveal the location of specific cellular components, a process that requires the fixation step. However, this methodology provides only a single instant in time for researchers to analyze. Sometimes this is sufficient. But in order to study the kinetics of a cellular event or track changes in a cell over time, the ability to image a live cell is paramount. Additionally, the process of preparing fixed cells has been found to cause artifacts that can confound the interpretation of the data.

Caveat emptor. Together with the clear advantages of live-cell imaging come new challenges. Dead cells can be treated relatively harshly without much concern. Live cells on the other hand, frequently require careful handling that includes a constant temperature, stable CO_2 levels, and sufficient nutrients. Moreover, the lasers used in many fluorescent microscopes to create the beautiful and colorful images we have come to know are so powerful that they can easily damage cells even during short-term illumination. Live-cell imaging is, in its most fundamental form, a constant balance between achieving the necessary data and not damaging or killing the cells.

A variety of clever solutions have been developed recently that surpass the methods and materials of yesteryear, including brighter fluorescent dyes that require lower-energy activation light, more sensitive detectors that can image both more quickly and in lower light, and techniques and technologies that use hardware and software tricks to minimize the amount of light bathing the sample. None of these provides a complete solution, but these advances and others have allowed researchers to better balance the best resolution, fastest imaging speed, maximum imaging depth, and best cell health to obtain the optimal results. The content provided in this new supplement gives you an indication of how they're succeeding in these efforts. We've provided three recent *Science* and *Science Advances* articles and an exclusive white paper in this timely update on live-cell imaging. We hope you enjoy reading it.

Sean Sanders, Ph.D.
Editor, *Science*/AAAS Custom Publishing Office

Shedding light on life

"A picture is worth a thousand words," goes the saying. As such, the evolution of humanity is tracked and studied by the drawings and pictures created by generations who sought to depict their world, and the accuracy and frequency of the images mark how well we were and are able to describe and understand the phenomena of the world.

Over the last two centuries the rapid progression of innovative microscopy techniques has allowed unprecedented visualization and description of microscopic phenomena, making a light microscope an indispensable tool in every biological or medical laboratory. As the light microscope has developed, it has given rise to hundreds of different imaging techniques, from brightfield and differential interference contrast to modern fluorescence and superresolution microscopy, which all have one thing in common: They are based on light and its interaction with the specimen. Nowadays light microscopes cannot match the resolution of electron microscopes or the penetration of X-ray microscopes, but they remain unchallenged when it comes to the imaging of dynamic processes in living cells, tissues, and organisms—observing life as it happens. Traditionally, light microscopes were divided into two distinct groups: widefield microscopes, which can acquire an entire image in a single exposure, and laser scanning microscopes, that image a specimen sequentially, point-by-point. While the latter produce crisper images of thick specimens, the former record images much faster and with less damage to the specimen.

Since Carl Zeiss, Ernst Abbe, and Otto Schott laid the foundations of modern microscopy 170 years ago, the company they founded delivered most of the radical microscope innovations, from the simple achromatic and apochromatic lenses of the 19th century, to the complex imaging instruments of today. The latest innovation from ZEISS is a novel confocal detector named Airyscan. It blurs the traditional divide between widefield and laser scanning microscopes and offers users the best of both worlds: high-speed, gentle imaging combined with superb resolution and contrast, capabilities unmatched by standard confocal microscopes.

We hope you will find this collection of publications and peer-reviewed articles interesting and inspiring, an example of how innovative light microscopy continues to enable researchers to push the boundaries of human knowledge. We believe that modern light microscopy can make a difference in your research as well. We are excited to contribute to your success.

Bernhard Zimmermann, Ph.D.
Senior Director Segment Marketing Life Sciences
Carl Zeiss Microscopy GmbH
microscopy@zeiss.com

Airyscan image of the central nervous system of a *Drosophila melanogaster* embryo.

Bringing cellular dynamics to light with live-cell microscopy

By Jeffrey M. Perkel

Light microscopy has countless applications in today's life sciences laboratory, from documenting cellular and organismal structure and mapping RNA localization, to tracking cellular dynamics. First, though, researchers must answer a fundamental question: Are they going to image the cells while they're alive, or after they're dead?

For many projects, the answer is: both. Yet the question defines the kind of data a microscope provides, and thus, the questions researchers can ask of it. Dead men tell no tales, as the saying goes, but dead cells do. Immunohistochemistry, for instance, reveals cellular and tissue morphology and protein distribution in fixed samples, while in situ hybridization reports the abundance and subcellular location of specific DNA or RNA sequences—data that pathologists can use to diagnose and stratify disease, among other things. Confocal and superresolution microscopy methods likewise have yielded up dazzling images of organismal and subcellular architecture from fixed cells, such as the 2013 discovery (using stochastic optical reconstruction microscopy, or STORM, superresolution microscopy) by Harvard University's Xiaowei Zhuang of a "periodic cytoskeletal structure" undergirding long axonal filaments—a subcellular protein scaffold that researchers never previously knew existed (*1*).

In all these cases, the data produced are static representations of once-living systems—the equivalent of reducing a movie to a single frame. And for many questions, the resulting data are good enough to provide the answers. But some questions simply cannot be answered from single images. In those cases, researchers turn to live-cell imaging.

In theory, live-cell microscopy is no different from any other microscopy method. But live cells do pose significant technical issues, and researchers pursuing live-cell methods have devised strategies for dealing with them.

The *sine qua non* of live-cell microscopy is, obviously, live cells, and both microscope vendors and third-party firms offer tools (such as climate-controlled growth chambers) to facilitate such research. But it's not enough that the cells be alive; generally they also have to be healthy, and not all microscopy techniques are compatible with that state. Fluorescence-based approaches, especially, often require extended and intense sample irradiation with high-powered light sources, which can induce phototoxicity. Fixed cells can easily stand this assault—so long as the fluorescent dyes or proteins being imaged do not succumb to negative effects such as photobleaching. But live cells can become stressed and apoptotic, or at the very least alter their behavior, under the blinding glare of such scrutiny.

"As part of their normal life cycle, most tissues and cells are never exposed to light, and it is known that ultraviolet (UV) light damages DNA, focused infrared (IR) light can cause localized heating, and fluorescence excitation causes phototoxicity to tissues and cells," wrote Clare Brown and colleagues of McGill University in a 2009 commentary in the *Journal of Cell Science* (*2*).

Live cells also move and change shape, as do their subcellular components, potentially complicating image collection and data analysis. Researchers are also limited in the types and nature of stains they can use to visualize those cells, and many fluorescent dyes are incompatible with live cells. As a result, live-cell imaging studies often employ fluorescent proteins rather than inorganic dyes or fluorophore-conjugated antibodies for staining purposes, or enzyme-based tags such as HaloTag, which allow researchers to label specific proteins in live cells (*3*).

IMAGE: COURTESY OF JULIA SELLIN, MICHAEL HOCH, LIMES INSTITUT, UNIVERSITY OF BONN

Researchers have no shortage of options for livecell microscopy, from standard brightfield and differential interference contrast microscopy, to confocal and superresolution approaches. Here, we consider some of the more popular fluorescence-based strategies.

The most straightforward approach, perhaps, is basic widefield fluorescence microscopy, in which an entire field of view is illuminated with excitation energy, and total fluorescence from the area is recorded at once using an area detector, such as a CCD (charge-coupled device) or CMOS (complementary metal-oxide semiconductor) camera. The simplest microscopy method available, widefield imaging also yields the blurriest images, as there's no mechanism to exclude out-of-focus light from reaching the detector. Thus, according to a review on the Carl Zeiss Microscopy Online Campus, "widefield imaging achieves the optimum results when the features of interest are either large (such as an organelle) or highly punctate in nature" (*4*).

One strategy for overcoming those limitations is confocal microscopy. A bright light source (usually a laser) is focused onto a particular point in the sample. The resulting fluorescence is then captured after it passes through a small pinhole aperture, which blocks out-of-focus light, producing a sharp image. The focal plane is then stepped perpendicular to the slide (i.e., along the *z* axis), creating multiple optical planes that can be virtually assembled to create a 3D representation of the original sample.

Confocal systems generally take one of two approaches to reconstruct each optical slice: Either the diffraction-limited illumination point is raster-scanned across the sample (as in laser-scanning confocal microscopy), or multiple points are imaged simultaneously (as in spinning-disk confocal microscopy). The difficulty is that whatever *z* position is being imaged, the entire sample volume is illuminated, increasing the likelihood of phototoxicity and photobleaching. The spinning-disk approach is generally considered faster and less phototoxic, but both can be applied to live cells, assuming the experiment is designed appropriately. Newer resonant scanning heads, such as that in the Nikon A1R+ confocal system can accelerate scanning-based microscopy to 30 frames per second or higher, depending on the size of the scanned region.

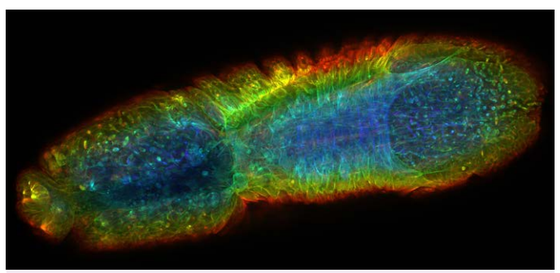

IMAGE: COURTESY OF BALAZS ERDI, MAX F. PERUTZ LABORATORIES, UNIVERSITY OF VIENNA AND MEDICAL UNIVERSITY OF VIENNA

A still from an 11-hour time lapse of *Drosophila melanogaster* embryogenesis imaged with Airyscan Fast. Mictrotubules labeled with green fluorescent protein (GFP); depth-coded maximum intensity projection.

One alternative to confocal microscopy is pairing widefield microscopy with deconvolution strategies. Widefield images typically subject cells to lower light intensity than confocal. But, since the resulting pictures tend to be blurrier, especially with thick specimens, they can be cleaned up using computational algorithms to produce a sharper reconstruction.

"Superresolution microscopy" is a catch-all term describing a half-dozen or so different methods.

Another alternative strategy, also compatible with live-cell imaging, is confocal microscopy using ZEISS's Airyscan detector. In a typical confocal, one or more pinholes are used to reject out-of-focus light; in-focus emission light is captured using a point detector (such as a photomultiplier tube) or spectral array. As a result, the researcher must balance signal with clarity: By making the pinhole smaller, image sharpness increases, but less light is captured, meaning more intense excitation light must be used. Airyscan circumvents that problem by eliminating the pinhole and projecting the emission light onto a 32-element array of hexagonal detectors. "Each detector element functions as a single, very small pinhole," according to company literature, leading to stronger signals, increased resolution, and decreased imaging speed.

"Superresolution microscopy" is a catch-all term describing a half-dozen or so different methods. In general, they also fall into two categories, the first of which includes localization-based approaches such as PALM (photoactivated localization microscopy) and STORM (available from ZEISS and Nikon, respectively). Normally, all fluorescent molecules in a diffraction-limited spot will fluoresce, making it impossible to differentiate fluorophores separated by less than about 200 nm. Localization-based approaches circumvent that problem by keeping most fluorophores dark and allowing only a stochastic handful to fluoresce. The positions of those fluors can then be mapped with subdiffraction resolution, at which point the process repeats until sufficient molecules have been mapped to reconstruct the original image. The second category of methods, which includes STED (stimulated emission depletion, available from Leica Microsystems), RESOLFT (reversible saturable optical fluorescence transitions), and SIM (structured illumination microscopy, available from ZEISS, Nikon, and GE Healthcare Life Sciences), use patterned light sources to define specifically where fluorophores are on and off.

Live-cell images have been collected with many of these different techniques. In one 2013 study, for instance, Nobel laureate Stefan Hell and colleagues at the Max Planck Institute for Biophysical Chemistry used a homemade RESOLFT system capable of producing 116,000 simultaneous "doughnuts" of light to capture neurite growth over nearly 4 minutes (*5*). In early 2016, Joerg Bewersdorf and colleagues at continued>

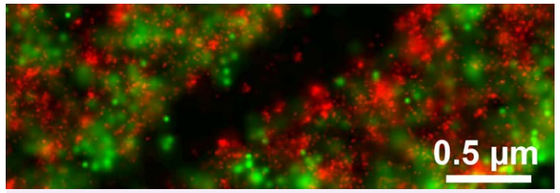

Dual-color PALM image of Chinese Hamster Ovary cells using fast sequential laser switching (Dronpa-Paxillin, red; tdEOS-Vinculin, green).

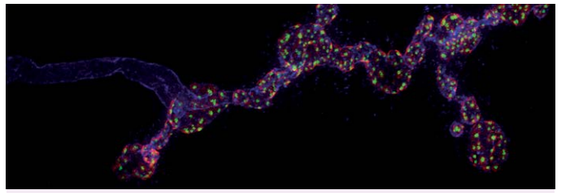

Superresolution SIM image of synapses at the neuromuscular junction in *Drosophila melanogaster.* Triple staining for the presynaptic active zone marker Brp (green), postsynaptic glutamate receptors (red), and the presynaptic membrane (blue).

Yale University described a method for two-color live-cell STED imaging using HaloTag- and SNAP-tag-based fluorophores, which they used to differentiate the lumen and membrane of the endoplasmic reticulum (*6*). And in 2012, Susan Cox and colleagues of King's College London developed a computational strategy called "Bayesian analysis of blinking and bleaching" (3B) that accelerated PALM to the point that the team could image structures called "podosomes" for about 100 seconds at 4-second resolution (*7*).

In general, however, the localization techniques are considered too slow for many live-cell applications (as many thousands of "frames" must be collected to reconstruct a single image), and often require light of such high intensity as to be phototoxic in many instances. The one exception is SIM, thanks to its speed and relatively gentle illumination conditions. But SIM also yields the lowest resolution of any superresolution method, about 100 nm.

In a 2015 report in *Science* detailing technical modifications that increase SIM resolution to between 84 nm and 45 nm, Janelia Research Campus investigator and Nobel Prize winner Eric Betzig detailed the difficulty of applying superresolution methods to live cells. Many such techniques, he wrote, "place extraordinary demands on the photon budget, represented by the product of the number of fluorescent molecules in the specimen and the number of photons each can emit before bleaching irreversibly. They also require specialized photoswitchable labels and excitation intensities of 10^3 to 10^8 W/cm^2, which are orders of magnitude greater than the 0.1 W/cm^2 under which life evolved" (*8*).

For those specifically interested in membrane dynamics, TIRF (total internal reflection fluorescence) microscopy is a popular live-cell imaging technique. In TIRF, excitation energy is directed at the glass-sample interface at an oblique angle such that it creates an evanescent wave parallel to the slide surface, extending only about 100 nm into the sample. As a result, only those fluorophores relatively near the slide surface will fluoresce, producing a sharper image. In one recent example, Lynn Enquist and colleagues at Princeton University used live-cell TIRF microscopy to image the exit of newly formed viral particles from cells (*9*).

A conceptually related idea is light-sheet microscopy. Here, rather than illuminating the entire sample volume (as in bright-field and confocal microscopy), specimens are hit with a thin planar "sheet" of light from the side and imaged from an orthogonal direction. By translating that sheet up and down, the system can then capture 3D volumes repeatedly over time, producing a 4D dataset. Commercial light-sheet implementations are available, but researchers can build their own using the detailed instructions laid out by the OpenSPIM (selective plane illumination microscopy) project (openspim.org).

Some researchers, though, need to up the ante. In late 2015, for instance, Philipp Keller and colleagues of the Janelia Research Campus described a custom microscopy system called "IsoView," which exploits two perpendicular light sheets to capture four separate images of a sample simultaneously. That strategy is particularly useful when imaging relatively opaque samples, such as *Drosophila* embryos, and the team used it to (among other things) track cellular motion during fruit fly gastrulation over a 3-hour period, collecting 3D volumes at 0.25 Hz (*10*).

Also at Janelia, in 2014 Betzig developed a higher-resolution light-sheet-based strategy called "lattice light-sheet microscopy." This approach differs from IsoView essentially in the thickness of the generated sheets and the resolution of the resulting images, and Betzig used it to image subcellular events in 3D over extended periods, including mitosis in HeLa cells (*11*).

Those researchers interested in imaging cells relatively deep within tissue sections and even live animals may benefit from two-photon or multiphoton microscopy. Like confocal and light-sheet microscopy, multiphoton microscopy creates thin optical sections in tissue (*12*). But it does so via a different mechanism, requiring the fluorophore to almost instantaneously absorb two low-energy photons to fluoresce rather than one high-energy photon.

This strategy offers several potential benefits. First, because multiple absorption events occur only in the focal plane, out-of-focus fluorophores remain dark in this method, not to mention unaffected by the incident light, thereby increasing signal-to-noise while minimizing photobleaching and phototoxicity. And, because the technique uses lower-energy, higher-wavelength light, that light can penetrate deeper into the tissue than most microscopy methods are capable of reaching—several hundred microns at least. That said, multiphoton microscopy traditionally suffers from a relatively low scan speed, slowing image capture. In one recent report, researchers at the University of Strathclyde in Scotland describe a widefield-based image-capture strategy to circumvent that problem, which they used to image calcium signaling events in rat neurons at up to 100 Hz (*13*).

IMAGES: (FROM TOP) COURTESY OF H. SHROFF, H. HESS, HHMI JANELIA FARM, ASHBURN, VIRGINIA, USA; COURTESY OF JAN PIELAGE, FRIEDRICH MIESCHER INSTITUTE, BASEL, SWITZERLAND

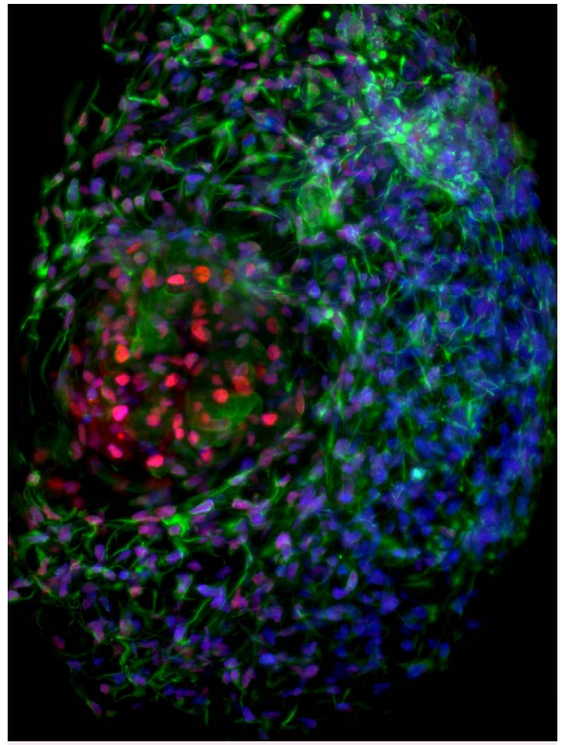

Light-sheet image of hepatocyte spheroids showing nucleus (HNF4a/HNF3b) and cytoskeleton (CK18) staining.

IMAGE: COURTESY OF JOHN TNG WEIQUAN, NG HUCK HUI, GENOME INSTITUTE OF SINGAPORE

When it comes to microscopy, there is no one perfect instrument for every occasion. Confocal microscopy excels at removing out-of-focus light, but that may not be absolutely necessary if you're imaging only very thin specimens. Superresolution microscopy yields magnificent detail, but that really only matters if the objects being studied are small enough or close enough together to be otherwise unresolvable.

Microscopy, in other words, is a balancing act. In a 2015 supplement to *Science*, Betzig described that balance in terms of a tetrahedron, with vertices representing spatial resolution, cell viability, imaging depth, and speed (*14*). *Science* writer Mike May, who interviewed Betzig, explains it thusly:

Imagine a point inside that tetrahedron as a representation of an imaging method's combination of features. If it improves one feature, say spatial resolution, it moves closer to that vertex and away from the others, thereby reducing its capabilities in the remaining three characteristics. To attain higher spatial resolution, for example, an imaging method requires more pixels, and that requires more measurements, which takes more time and might damage the cells by exposing them to more light.

Conversely, an imaging approach that is very fast must, by necessity, not linger over any one position, meaning that fewer photons will be collected, causing signal-to-noise to suffer—unless brighter excitation light is used.

Microscopists are no stranger to this tug-of-war—it's one of the reasons most research institutions contain microscopy core facilities stocked with multiple instruments (economic considerations being another key factor, of course). And in many cases, researchers can obtain sufficient quality data out of whatever instrument they have available, even if it isn't the top-of-the-line hardware.

The good news for researchers is this: With so many tools in the toolbox, finding the right one for your imaging needs is easier than ever.

Jeffrey M. Perkel is a freelance science writer based in Pocatello, Idaho.

References

1. K. Xu, G. Zhong, X. Zhuang, Actin, spectrin, and associated proteins form a periodic cytoskeletal structure in axons. *Science* **339**, 452–456 (2013).
2. M. M. Frigault *et al.*, Live-cell microscopy—tips and tools. *J. Cell Sci.* **122**, 753–767 (2009).
3. J. B. Grimm *et al.*, A general method to improve fluorophores for live-cell and single-molecule microscopy. *Nat. Methods* **12**, 244–250 (2015).
4. M. E. Dailey *et al.*, Live-cell imaging techniques. Carl Zeiss Microscopy Online Campus, available at http://zeiss-campus.magnet.fsu.edu/articles/livecellimaging/techniques.html.
5. A. Chmyrov *et al.*, Nanoscopy with more than 100,000 'doughnuts.' *Nat. Methods* **10**, 737–740 (2013).
6. F. Bottanelli *et al.*, Two-colour live-cell nanoscale imaging of intracellular targets. *Nat. Commun.* **7**, 10778 (2016).
7. S. Cox *et al.*, Bayesian localization microscopy reveals nanoscale podosome dynamics. *Nat. Methods* **9**, 195–200 (2012).
8. D. Li *et al.*, Extended-resolution structured illumination imaging of endocytic and cytoskeletal dynamics. *Science* **349**, aab3500 (2015).
9. I. B. Hogue *et al.*, Cellular mechanisms of alphaherpes virus egress: Live cell fluorescence microscopy of pseudorabies virus exocytosis. *PLOS Pathog.* **10**, 1004535 (2014).
10. R. K. Chhetri *et al.*, Whole-animal functional and developmental imaging with isotropic spatial resolution. *Nat. Methods* **12**, 1171–1178 (2015).
11. B.-C. Chen *et al.*, Lattice light-sheet microscopy: Imaging molecules to embryos at high spatiotemporal resolution. *Science* **346**, 1257998 (2014).
12. R. K. P. Benninger, D. W. Piston, Two-photon excitation microscopy for the study of living cells and tissues. *Curr. Protoc. Cell Biol.* **59**, 4.11.1–4.11.24 (2013).
13. R. Amor *et al.*, Widefield two-photon excitation without scanning: Live cell microscopy with high time resolution and low photo-bleaching. *PLOS ONE* **11**, e0147115 (2016).
14. M. May, Top tips from the superresolution microscopy pros, in Microscopy now: Getting the most from your imaging, pp. 13–16. Sponsored supplement to *Science*, Oct. 2 (2015).

RESEARCH ARTICLES

MICROTUBULES

Detyrosinated microtubules buckle and bear load in contracting cardiomyocytes

Patrick Robison,[1] Matthew A. Caporizzo,[2] Hossein Ahmadzadeh,[2] Alexey I. Bogush,[1] Christina Yingxian Chen,[1] Kenneth B. Margulies,[3] Vivek B. Shenoy,[2] Benjamin L. Prosser[1]*

The microtubule (MT) cytoskeleton can transmit mechanical signals and resist compression in contracting cardiomyocytes. How MTs perform these roles remains unclear because of difficulties in observing MTs during the rapid contractile cycle. Here, we used high spatial and temporal resolution imaging to characterize MT behavior in beating mouse myocytes. MTs deformed under contractile load into sinusoidal buckles, a behavior dependent on posttranslational "detyrosination" of α-tubulin. Detyrosinated MTs associated with desmin at force-generating sarcomeres. When detyrosination was reduced, MTs uncoupled from sarcomeres and buckled less during contraction, which allowed sarcomeres to shorten and stretch with less resistance. Conversely, increased detyrosination promoted MT buckling, stiffened the myocyte, and correlated with impaired function in cardiomyopathy. Thus, detyrosinated MTs represent tunable, compression-resistant elements that may impair cardiac function in disease.

Along with its well-defined transport functions, the microtubule (MT) network serves multiple mechanical roles in the beating cardiomyocyte. MTs function as mechanotransducers, converting changing contractile forces into intracellular signals (*1*, *2*). MTs may also act as compression-resistant elements, which could provide a mechanical impediment to cardiomyocyte contraction (*3*–*5*). If so, they must bear some of the compressive and tensile load of a working myocyte. Unfortunately, little is known about MT behavior during the contractile cycle. During this cycle, Ca^{2+}-mediated actin-myosin interaction first shortens repeating contractile units called sarcomeres, which are then stretched as the heart fills with blood during diastole.

Although an isolated MT would present minimal resistance to myocyte compression, the stiffness of the network within a living cell, with MT-associated proteins and other cytoskeletal elements, can change by orders of magnitude (*6*, *7*). It is in this context that MTs are proposed to act as compression-resistant elements (*6*, *8*) that may impair sarcomere shortening and thus cardiac function, particularly in disease states associated with MT proliferation (*8*–*10*). Posttranslational modification (PTM) of MTs (*11*, *12*) could also modify their mechanical properties and binding interactions. Detyrosination, a PTM of α-tubulin, has recently been shown to augment MT-dependent mechanotransduction in dystrophic cardiac and skeletal muscle (*12*). This specific PTM is also increased in animal models of heart disease (*1*, *13*, *14*), which raises a mechanistic question: If mechanosignaling is altered, have the mechanical properties of the myocyte changed?

Although the idea that a proliferated (and perhaps modified) MT network may mechanically interfere with contraction is attractive, the "MT hypothesis" has remained controversial [for reviews, see (*15*, *16*)]. Two important limitations have hindered our understanding: (i) a reliance on blunt pharmacological tools (colchicine/Taxol) that have off-target consequences; (ii) a lack of direct observation of MTs under the stress and strain of the contractile cycle. Here, we characterized MTs under contractile loads using a high-resolution imaging technique and directly tested how MT detyrosination may regulate load-bearing and the mechanical properties of the myocyte.

MTs buckle under contractile load

MT networks in cardiomyocytes have two major features (Fig. 1A): an orthogonal grid just beneath the membrane that wraps the myofibrils and a deeper network composed primarily of longitudinal elements that interdigitate the myofibrils. Longitudinal MTs often run many sarcomeres in length but do not span the full cell. Given that cardiomyocytes change shape during contraction, the MT cytoskeleton must accommodate this change. There are three apparent possibilities: MTs not anchored to other cytoskeletal or sarcomeric proteins could rearrange or slide passively with the surrounding medium; anchored MTs could directly experience contractile force and themselves deform under load; or the MTs could break and/or disassemble and reform. These possibilities offer divergent mechanisms for the regulation of mechano-signaling and the overall mechanics of the myocyte. Without direct observation, however, this behavior has been difficult to quantify.

Standard confocal imaging, although capable of resolving MTs in living cells (*17*), suffers from limitations in the signal-to-noise ratio when pushed to speeds that can resolve events on the time scale of cardiomyocyte contraction (Fig. 1B and movie S1). Consequently, we turned to a high-speed, subdiffraction limit technique called Airyscan (see fig. S1). This technology maintains high signal-to-noise ratios at the required temporal resolution, while offering a 1.7-fold improvement in spatial resolution beyond the standard diffraction limit.

Using the MT-binding fluorogenic dye SiR tubulin, based on the fluorophore silicon rhodamine (*18*) (Fig. 1C and movie S2), we imaged internal MTs during contractions triggered by a 1 Hz electrical field stimulation in isolated mouse cardiomyocytes. We were able to capture MT behavior during contraction and found that longitudinally oriented MTs frequently deformed and developed sinusoidal buckles. Because SiR tubulin may polymerize MTs (*18*), we also generated adenovirus encoding a small fragment of the MT-binding protein ensconsin fused to three copies of GFP (EMTB-3xGFP) to decorate MTs. We achieved similar results (table S1) but with improved signal-to-noise ratios (Fig. 1D and movie S3).

We measured blindly selected MTs for deformation with two parameters—amplitude and wavelength (Fig. 1G). Where possible, the same MT was followed through contraction. Amplitude rose quickly from resting to contracted levels (Fig. 1H), with clearly visible buckles. Using a threshold of two standard deviations above resting amplitude, we found that two-thirds of MTs buckle under control conditions (Fig. 1H).

MT buckles quickly reversed during relaxation, and the configuration of the MT network between contractions tightly colocalized with the network configuration from previous cycles (Fig. 1, E and F), with a minimal mean reduction in Pearson's colocalization of 0.01 per contractile cycle (n = 18 runs). The rapid and precise reversibility of the network deformations suggested tight coupling to the contractile apparatus, and it argues against MT breakage and regrowth contributing to mechanical properties and signaling over the time scale of myocyte contraction.

A notable feature of the MT buckles was the emergence of subpopulations of buckle wavelength centered at ~1.65 μm, 3.3 μm, and perhaps even 4.7 μm (Fig. 1I). These corresponded closely to the length of one, two, or three contracted sarcomeres, respectively. Although MTs buckling outside of these populations could be found in our data without difficulty, these subpopulations were strongly

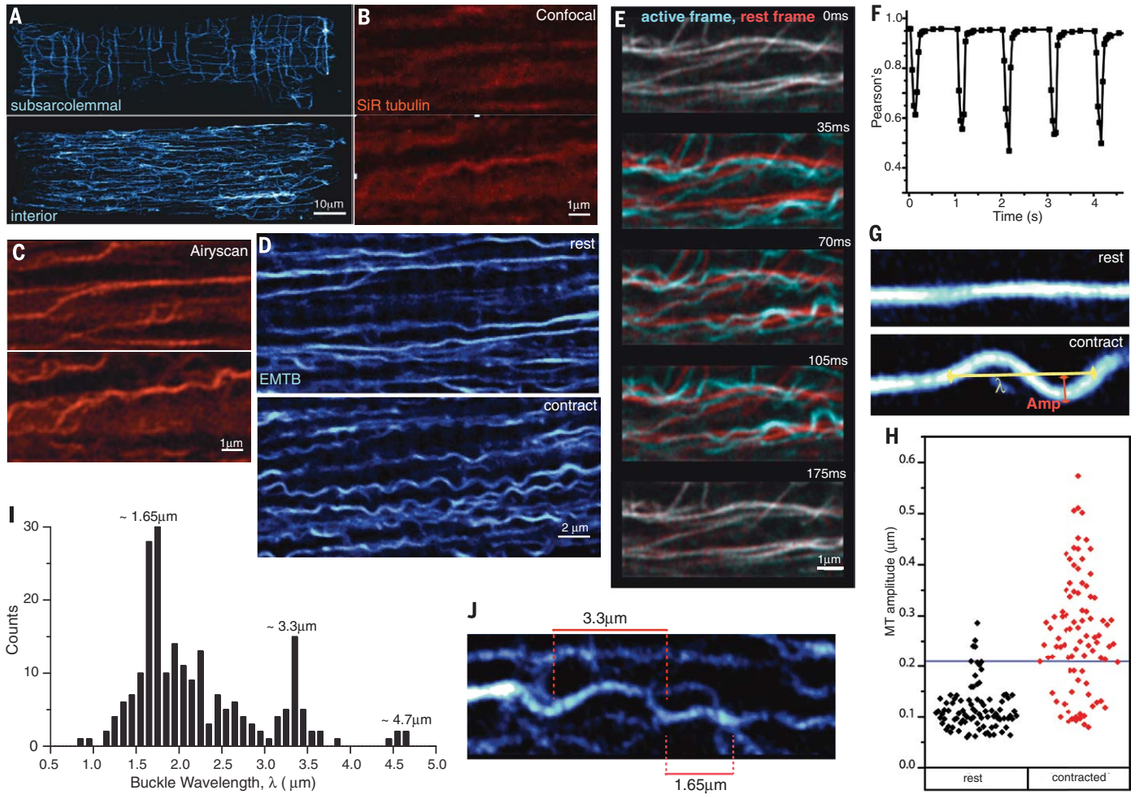

Fig. 1. MTs reversibly buckle in contracting cardiomyocytes. (**A**) The subsurface (top) and interior (bottom) cardiomyocyte MT network. (**B**) High-speed confocal imaging of MTs at rest (top) and during contraction (bottom) labeled with SiR tubulin with brightness increased for comparison with (C). (**C**) Airyscan imaging of the same MTs as in (B) at rest and during contraction. (**D**) Wider view of MTs labeled with EMTB-3xGFP at rest (top) and during contraction (bottom). (**E**) MTs imaged throughout a contractile cycle (cyan) were overlaid onto the network configuration from the initial frame at rest (red). (**F**) Colocalization analysis of (E) shows that MTs repeatedly return to the same position. Pearson's coefficient is used to estimate goodness of fit to original MT configuration over several contractile cycles. Initial drop to ~0.96 is due to imaging noise. (**G**) Quantification of buckling amplitude (measured from centerline to edge) and λ (wavelength measured as twice the distance between consecutive inflection points). (**H**) Amplitude of MTs labeled with EMTB-3xGFP in resting (black) and contracted (red) cardiomyocytes. The threshold to determine buckling occurrence (blue line) was two standard deviations above the mean resting value. (**I**) Distribution of buckling wavelengths in cardiomyocytes shows a dominant population between 1.6 and 1.7 μm, and a second population at 3.3 μm. (**J**) A representative MT demonstrating buckles with wavelengths that correspond to the distance between one (1.65 μm) or two (3.3 μm) adjacent sarcomeres.

indicative of ordered geometric constraints on the buckling MT. This was observed in certain cells where faint transverse staining at the Z-disc shows MTs buckling between sarcomeric constraints (movie S4).

Detyrosination regulates MT buckling in the heart

This robust buckling behavior of the MT network may be a result of a particularly high abundance of "detyrosinated" MTs in adult cardiomyocytes (*19*). Detyrosination is a PTM of α-tubulin where the C-terminal tyrosine residue has been cleaved by a tubulin carboxypeptidase (TCP); this process can be readily reversed by tubulin tyrosine ligase (TTL) (*11*). This tyrosination cycle is evolutionarily conserved across eukaryotes (*20*) and appears required for life (*21*), yet its functional roles are still poorly understood. Because detyrosination can protect MTs from disassembly (*22*, *23*) and can facilitate their cross-linking with intermediate filaments (IFs) (*24*, *25*), we hypothesized that the high proportion of detyrosination may confer the resilient load-bearing capabilities of the cardiac cytoskeletal network.

Using antibodies specific to detyrosinated α-tubulin, we found a high abundance of detyrosination in the α-tubulin network of adult myocytes (Fig. 2, A and B), as expected (*12*, *19*). To test the role of detyrosinated MTs, we generated adenovirus encoding TTL (AdV-TTL) with a *Discosoma* red fluorescent protein (DsRed) reporter. Expressing this construct in isolated cardiomyocytes could effectively reduce the level of detyrosination as shown by both immunofluorescence (Fig. 2, A and B) and immunoblot (Fig. 2, C and D), which resulted in a 71% reduction in the amount of polymerized, detyrosinated MTs, with a concomitant up-regulation of tyrosinated tubulin (Fig. 2, C and D, and fig. S2). Overexpression of TTL also resulted in a modest (10%) reduction in the density of the polymerized MT network (Fig. 2B), consistent with an increased disassembly of tyrosinated MTs (*22*, *23*). We complemented this genetic strategy with a pharmacological approach to inhibit TCP using parthenolide (PTL) (*26*). PTL treatment also reduced the fraction of detyrosinated MTs, albeit to a lesser extent (42%) than

[1]Department of Physiology, Pennsylvania Muscle Institute, University of Pennsylvania Perelman School of Medicine, Philadelphia, PA 19104, USA. [2]Department of Materials Science and Engineering, University of Pennsylvania School of Engineering and Applied Science, Philadelphia, PA 19104, USA. [3]Department of Medicine, University of Pennsylvania Perelman School of Medicine, Philadelphia, PA 19104, USA.
*Corresponding author. Email: bpros@mail.med.upenn.edu

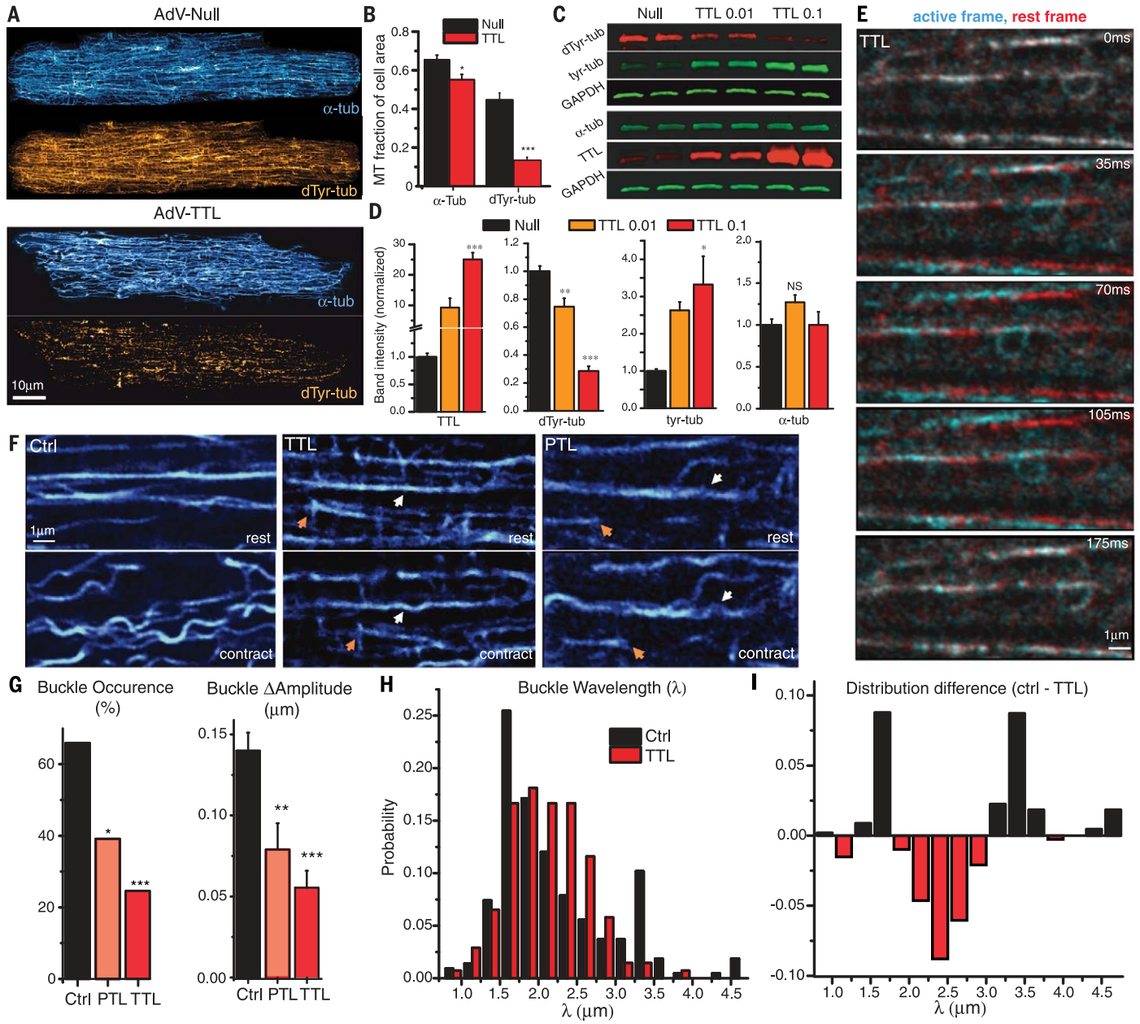

Fig. 2. Detyrosination underlies MT buckling. (**A**) The MT cytoskeleton (blue and aqua) in rat adult cardiomyocytes (top) is heavily detyrosinated (orange). TTL overexpression (bottom) reduces detyrosination dramatically but makes comparatively small changes in the overall MT network. (**B**) Quantification of the fraction of cell area covered by α-tubulin and detyrosinated tubulin (dTyr-tubulin) in null (n = 14) and TTL-overexpressing (n = 13) cells, as determined from thresholded images as shown in fig. S2E. (**C** and **D**) Western blots from cardiomyocyte lysates show the effects of viral overexpression of TTL. GAPDH, glyceraldehyde-3-phosphate dehydrogenase. (**E**) Time course of MTs in a contracting cardiomyocyte (cyan) transduced with AdV-TTL overlaid on the resting MT configuration (red). MTs appear to translocate along the contractile axis rather than deforming. (**F**) Comparison of MTs in resting (top) and contracted (bottom) cardiomyocytes in control, TTL, and PTL groups. In TTL and PTL groups, some MTs slide (orange arrows) relative to others that deform (white arrows). Additional examples are provided in fig. S3. (**G**) Buckling occurrence and amplitude are reduced by overexpression of TTL or treatment with PTL. (**H**) Buckling wavelength distribution in control and TTL-overexpressing myocytes and (**I**) the difference between these distributions. Overexpression of TTL causes MTs to buckle more often at wavelengths between 2 and 3 μm, and MTs are far less likely to buckle at distinct sarcomeric wavelengths (1.7 and 3.3 μm) when detyrosination is reduced. Data are presented as means ± SEM; $^{*}P < 0.05$, $^{**}P < 0.01$, $^{***}P < 0.001$. Further statistical details are available in table S1.

AdV-TTL and with no effect on MT network density (fig. S2).

The load-bearing behavior of the MT network in cardiomyocytes overexpressing TTL or treated with PTL was dramatically different from control myocytes. Tyrosinated MTs frequently seemed to simply slide in the moving cell (Fig. 2, E and F, orange arrows; movies S5 and S6; and fig. S3), rather than buckling under load. This behavior was again reversible, with a minimum reduction in Pearson's colocalization over successive contractions that was not different from controls (P = 0.87, n = 19 runs). The occurrence of buckling in TTL-overexpressing and PTL-treated cells fell significantly (Fig. 2G, left), whereas amplitude changes observed on the same MT between rest and contraction also dropped significantly (Fig. 2G, right, and table S1).

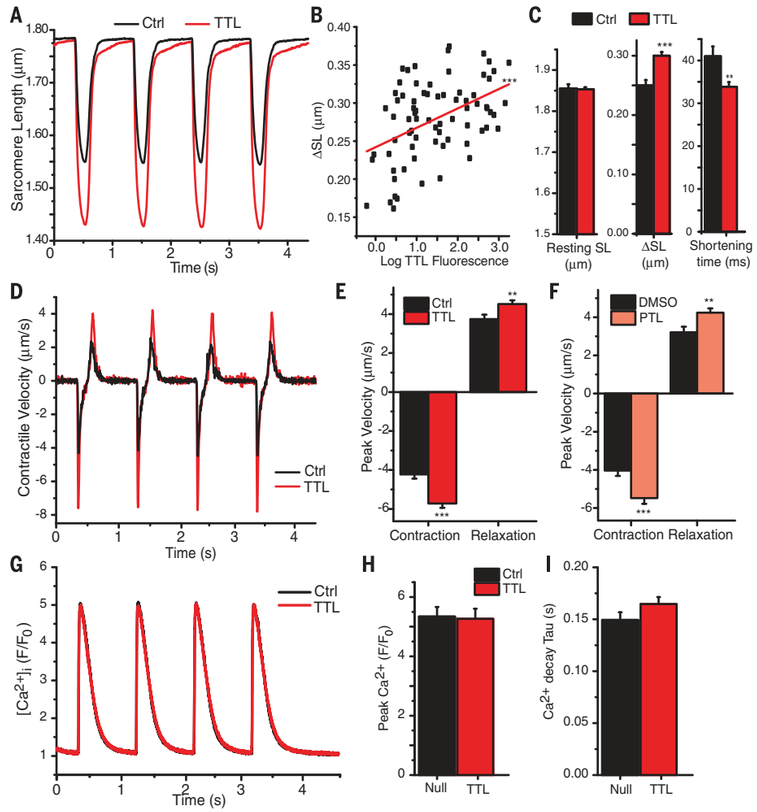

Fig. 3. Detyrosinated MTs impede contractility. (**A**) Sarcomere shortening (ΔSL) during contraction is increased in TTL-overexpressing myocytes. This change is (**B**) dose-dependent [$P = 1.2 \times 10^{-5}$, correlation coefficient (r^2) = 0.23] and (**C**) associated with a faster shortening time without affecting resting sarcomere length. (**D**) First derivative of traces in (A) demonstrate contractile velocities in control and TTL-overexpressing myocytes. (**E**) TTL-overexpressing myocytes demonstrate an increase in the peak velocity of both contraction and relaxation. (**F**) PTL-treated cells display similar behavior. (**G** to **I**) Despite the significant changes in contractility, no changes in the peak or kinetics of the global calcium transient were observable. F/F_0, the change in fluorescence from the original fluorescence before stimulation. Data are presented as means ± SEM; $^{*}P < 0.05$, $^{**}P < 0.01$, $^{***}P < 0.001$. Further statistical details are available in table S2.

When MT buckling was observed, the mean wavelength was not significantly different between control and TTL-overexpressing cells (table S1). However, the majority of MTs in TTL-overexpressing myocytes no longer buckled at the wavelength of a single sarcomere, and no subpopulations at multiples of the sarcomeric period were observed (Fig. 2H). Instead, the majority of these MTs buckled in a single population at wavelengths between 2 and 3 μm, which suggested that MT buckling was less constrained by a sarcomeric interaction after detyrosination was reduced (Fig. 2I).

Detyrosinated MTs resist contractile compression

The energy required to deform detyrosinated MTs under compressive load could confer some meaningful resistance to myocyte contraction. We thus tested directly if MT detyrosination affects contractility in beating cardiomyocytes. After overexpression of TTL, we found significant enhancements in both the magnitude (Fig. 3, A to C) and peak rate (Fig. 3, D and E) of sarcomere shortening (table S2). PTL had a similar effect on contractility (Fig. 3F and table S2). Peak relaxation rates were also increased, which could be because of a decrease in cellular viscosity (see below) or may reflect the increased magnitude of shortening and, therefore, compression of internal elastic elements (e.g., titin) that develop restoring force (*27*). These contractile changes were not associated with any significant difference in global calcium transients (Fig. 3, G to I) or resting sarcomere length (Fig. 3C), which suggested a change in intrinsic mechanical resistance associated with the ability of detyrosinated MTs to bear compressive load.

Detyrosination regulates myocyte mechanical properties

We next measured mechanical resistance directly using atomic force microscopy (AFM). AFM measurements of transverse stiffness were performed across a range of indentation rates. Myocyte stiffness changed substantially with indentation rate and was well fit by a standard linear solid model (SLSM) [methods in supplementary materials (SM)] (fig. S4 and Fig. 4A). At low rates (100 nm/s), the stiffness of the cardiomyocyte was essentially elastic, reported as E1, and was reduced by PTL treatment and TTL overexpression (Fig. 4B). At higher rates, the modulus increased by E2, which reflects cross-linked material inside the cell that slips on the time scale of slower measurements but "turns on" (stiffens) at faster time scales (> 2 μm/s) (*28*). The viscosity derived by the SLSM defines the rate above which these cross-links are engaged. TTL overexpression significantly decreased E2 and viscosity (Fig. 4B), which suggested that reducing detyrosination decreases the number of cross-links engaged at physiological strain rates in the cardiomyocyte.

The fact that MTs deform under load and resist sarcomere shortening implies a transfer of force between MTs and the sarcomere. If MTs resist longitudinal compression, they could also confer a tensile resistance when the sarcomeres are stretched, as occurs during diastolic filling. To test this idea, we measured passive stiffness directly along the longitudinal axis of TTL-overexpressing myocytes. We attached cardiomyocytes to laser-etched cell holders (Fig. 4C, fig. S5, and movie S7) via a biological adhesive (*1*) and subjected them to steplike changes in length, while simultaneously measuring sarcomere length and passive force with a high-sensitivity transducer (Fig. 4D). A typical force response (Fig. 4D, blue) showed a rapid rise to peak force during the high-velocity stretch (F_{peak}), containing both elastic and viscous elements, followed by a relaxation to a steady-state force ($F_{s.s.}$) that largely reflects the elastic stiffness of the myocyte. For a given step size, TTL-overexpressing myocytes exerted significantly reduced peak forces during physiological length changes, with modest reductions in steady-state force (fig. S5F). The TTL-overexpressing cells also underwent significantly larger changes in sarcomere length with any given step (fig. S5G), which indicated increased sarcomere compliance and which suggested that stiffer sarcomeres in control cells distribute the length change to other compliant components in series. As can be surmised from fig. S5, F and G, TTL overexpression decreased tension across the physiological range of sarcomere lengths achieved during diastolic filling (Fig. 4E), which indicated a role for detyrosinated MTs as tensile-resistant elements. Visual evidence supporting such a relation was seen in MT networks in a control cell at resting and stretched length (fig. S5 and Fig. 4C, cyan). At resting length, there was some inherent slack in the MT network, whereas the same MTs became

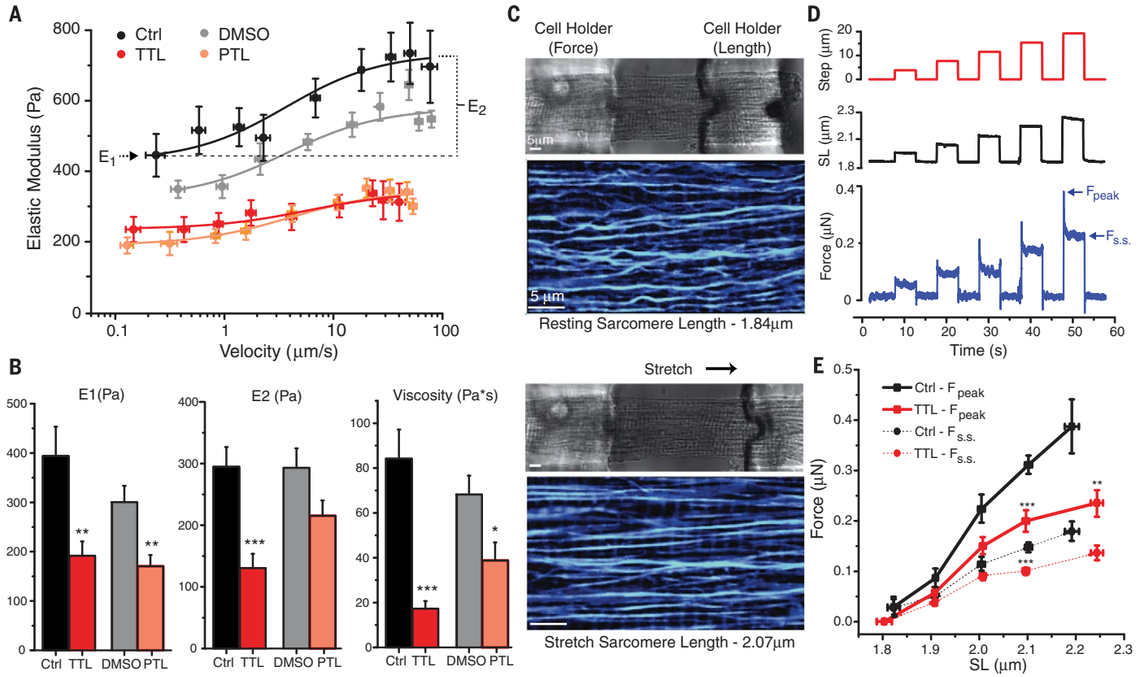

Fig. 4. Detyrosinated MTs regulate the viscoelasticity of cardiomyocytes. (**A**) Elastic modulus of cardiomyocytes measured by AFM at various indentation velocities and fit to SLSM (see methods in SM). (**B**) Quantification of velocity-independent (E1) and velocity-dependent (E2) components of the elastic modulus, and SLSM fit–derived viscosity. Both TTL overexpression and PTL treatment significantly reduced elasticity and viscosity. There were no significant differences in these parameters between dimethyl sulfoxide (DMSO) (gray) and AdV-null (black) transduced cells (P = 0.28, 0.34, and 0.33, respectively). Reductions in stiffness due to TTL overexpression are also apparent in cells under stretch along the longitudinal axis. (**C**) Myocytes were attached via glass cell holders (C, top, and fig. S5) to a force transducer and length controller and were subjected to stretch. MTs visualized by EMTB-3xGFP (C, blue and aqua) at rest (top) and at a stretched length (bottom). (**D**) Representative force versus length protocol. A series of stepwise stretches (red) in 4-μm increments are applied to an isolated myocyte, which increases sarcomere length (SL, black). Passive tension (blue) generated by the step relaxes quickly from a peak value to a new steady state. (**E**) Force measurements binned according to measured change in sarcomere length with a given step size. TTL-overexpressing cells exert reduced peak passive tension during step changes in length, with a more modest reduction in steady-state tension. Data are presented as means ± SEM; $*P < 0.05$, $**P < 0.01$, $***P < 0.001$. Further statistical details are available in tables S3 and S4.

taut when the cell was stretched and held at long sarcomere lengths (movie S8).

Model of MT contribution to cardiac contractility

We next sought to develop a mathematical model to recapitulate the experimentally measured changes in MT buckling and contractility when detyrosination is reduced. Previous work modeling MT buckles (*6*) suggests that three critical variables determine buckling behavior; MT stiffness, stiffness of the surrounding medium, and force incident on the long axis of the MT. How these three variables are predicted to alter MT behavior and myocyte mechanics is described in fig. S6. Of the three, only a decrease in incident force can explain our experimental observations after suppressing detyrosination. If MT anchoring to the sarcomere is disrupted, the reduced incident force on the MT may drop below the critical force required for buckling, which results in simultaneous decreases in buckling amplitude (Fig. 2) and viscoelasticity (Figs. 3 and 4). The sarcomeric periodicity of buckles (Fig. 1I) also suggests an underlying structural constraint that changes in MT or medium stiffness alone cannot explain. We thus chose to model MT buckling within a contractile model that includes a MT compression-resistive element that's interaction with the sarcomere can be varied (see model in SM for details).

Using the mechanical scheme detailed in Fig. 5A, we fitted the contraction resulting from a log-normal force input to derive both contractile and buckling parameters. By modifying the incident force applied to a MT for a given amount of sarcomere shortening (Fig. 5A and model in SM), we simulated the effect of a sarcomeric anchor sliding and then catching at detyrosinated regions of the MT. Inclusion of a 100-nm slide (50 nm at each anchor, see model) before MTs engage with the rest of the sarcomere is reasonable, given the ~80% reduction in detyrosinated area observed by immunofluorescence with TTL overexpression (Fig. 2C), and reflects the fact that reductions in detyrosination would increase the average distance between detyrosinated tubulins that could interact strongly with MT anchoring points. This disruption of MT-sarcomere coupling produced model outputs (Fig. 5, C and D) that closely recapitulated our experimental contractility and buckling results.

An alternate possibility to the sliding anchor is that the anchor is completely uncoupled by suppressing detyrosination and reverts to buckling behavior governed by local viscoelasticity rather than underlying structure, as proposed for less rigidly organized cell types, including developing myocytes (*6*). In either case, the coupling of MTs to the sarcomere is reduced, which impairs their ability to resist contraction.

Potential role for desmin as a sarcomeric MT anchor

The putative characteristics of the anchor—a mechanically stiff protein capable of forming complexes with MTs and restricted to a spatially defined region of the sarcomere—suggested the intermediate filament desmin as an immediate candidate.

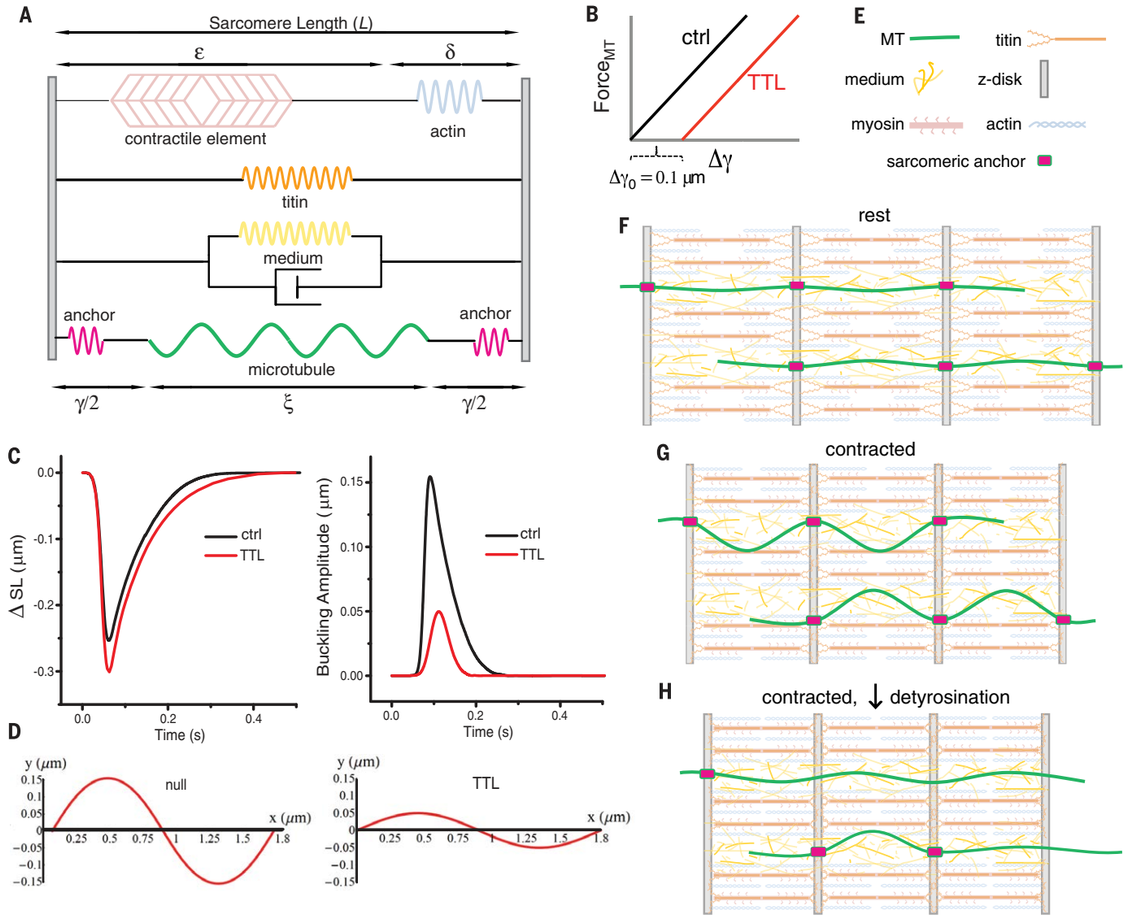

Fig. 5. Modeling MTs in the contracting sarcomere. (**A**) Mechanical schematic of the modeled sarcomere. A force-generating contractile arm (top) is coupled in parallel at the Z-disc to a spring element representing titin (orange), a viscoelastic medium (yellow spring and dashpot), and a MT (green) with anchors (fuschia pink) to the Z-disc (gray). The anchor to the Z-disc is only engaged at regions of MT detyrosination. (**B**) TTL overexpression is modeled by allowing the anchors to slide for 50 nm at each end before engaging and transmitting force to the MT at a detyrosinated subunit. (**C**) The change in sarcomere length at peak contraction and buckling amplitude. (C) and (**D**) recapitulate experimental observations for TTL-overexpressing myocytes after this change. (**E** and **F**) The cardiac sarcomere, shown with MTs with putative stiff anchors to the sarcomere, here, at the Z-disc. Contraction reduces the distance between anchor points, which requires the MTs either to buckle (**G**) if the anchors are engaged or to slide (**H**), if the anchors are not engaged and force incident on the MT remains low. Mathematical model parameters are available in table S5.

Desmin forms structural bundles that form a complex with the Z-disc (*29*), and intermediate filaments can form detyrosination-dependent cross-links with MTs (*30*, *31*).

We first sought to determine whether desmin preferentially associates with detyrosinated MTs. Cosedimentation of cardiomyocyte lysates showed that desmin forms pellets with polymerized MTs (Fig. 6A) in direct proportion to their level of detyrosination (Fig. 6, B and C), which indicated a specific and sensitive interaction. We also co-stained cardiomyocytes from desmin-depleted [knockout (KO)] and wild-type (WT) mice for desmin and both tyrosinated and detyrosinated tubulin to observe any preferential interaction. The two populations of MTs show similar overall patterning in WT myocytes, except for a specific accumulation of detyrosinated (and not tyrosinated) tubulin in transverse bands at the Z-disc that colocalized with desmin (Fig. 6, D and E, and fig. S7). Note that KO animals lacked this transverse pattern completely (Fig. 6D and fig. S7H), although the Z-disc itself remained intact (fig. S7C). In addition, KO myocytes had a denser (fig. S7F) and more disorganized MT network (fig. 6D and fig. S7, B and E), which suggested that desmin is required for proper MT network organization.

If desmin cross-links with detyrosinated MTs to structurally reinforce the network, then the removal of desmin should both decrease cytoskeletal stiffness and prevent tyrosination-dependent changes in viscoelasticity. Blind studies in WT and KO myocytes revealed that desmin KO myocytes were significantly less stiff than WT counterparts (Fig. 6, F and G), and that treatment with PTL no longer reduced viscoelasticity (Fig. 6, F and G).

MT detyrosination is sufficient to impair cardiomyocyte contractility

Increasing detyrosination correlates with impaired function in animal models of heart disease (*13*, *14*). Thus, we next tested whether increasing detyrosination could directly impair cardiac contractility.

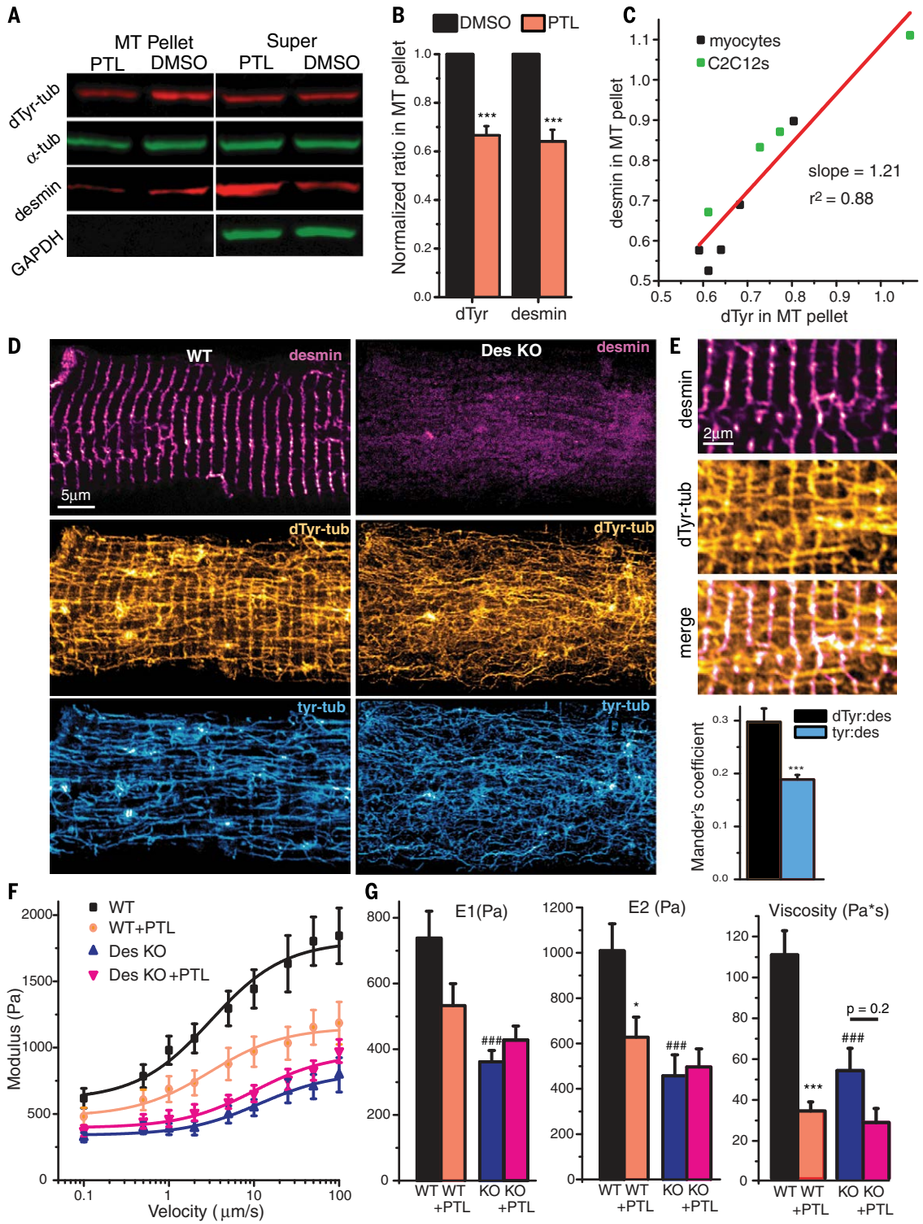

Fig. 6. Desmin associates with detyrosinated MTs to increase cardiomyocyte stiffness. (**A**) MT cosedimentation shows the interaction between polymerized MTs (pellet) and desmin. (**B**) Quantification of the amount of detyrosination and desmin (relative to the total amount of tubulin) in the MT pellet from cardiomyocyte lysates with and without PTL treatment. Data were normalized to DMSO level. (**C**) The amount of desmin associated with the MTs after PTL treatment is directly proportional to the amount of MT detyrosination across several experiments in rat cardiomyocytes and C2C12 cells. (**D**) Immunofluorescence of desmin, dTyr, and Tyr-tubulin shows dTyr-specific transverse pattern in WT, but not desmin KO, myocytes. (**E**) Overlay of dTyr-tubulin and desmin. (See fig. S7 for more examples.) (**F** and **G**) AFM measurements show a PTL-dependent reduction in myocyte stiffness and viscosity in WT, but not desmin, KO myocytes. Viscoelasticity in desmin KO myocytes is not statistically different from WT with PTL treatment. Data are presented as means ± SEM; *P < 0.05, **P < 0.01, ***P < 0.001 with respect to DMSO treatment; ###P < 0.001 with respect to untreated WT myocytes. Further statistical details are available in table S6.

Using an adenoviral construct expressing short hairpin RNAs (shRNAs) against TTL (shTTL), we suppressed TTL expression, which enhanced detyrosination (Fig. 7A and fig. S8). shTTL-transduced myocytes were then tested for their viscoelastic and contractile properties. The excess detyrosination alone was sufficient to increase viscosity and stiffness (Fig. 7, B and C) and suppressed contractile velocity and magnitude (Fig. 7, D and E).

We next examined whether this modification correlated with functional deficits in human heart disease. To this end, we analyzed left ventricular tissue samples from healthy patient donors and from patients exhibiting varying degrees of heart disease due to several underlying causes (table S7). Detyrosinated tubulin was significantly increased in patients with clinically diagnosed hypertrophic and dilated cardiomyopathies (HCM and DCM, respectively), along with a modest increase in total tubulin content (Fig. 7, F and G). Blind analysis of HCM patient data showed that detyrosination inversely correlated with left ventricular ejection fraction (LVEF), a primary indicator of cardiac contractility (Fig. 7H). There was no such correlation detected between LVEF and total or tyrosinated tubulin levels, nor any correlation between heart weight and detyrosination (fig. S9), which suggested a specific link between detyrosination and LVEF. Myocardium from patients with DCM all demonstrated considerably depressed LVEF and variable, but increased, detyrosinated tubulin.

TTL was unchanged in all patient populations, which showed that a decreased expression of the tyrosinating enzyme does not explain the increase in detyrosinated tubulin in patients with heart disease (Fig. 7G). Because the molecular

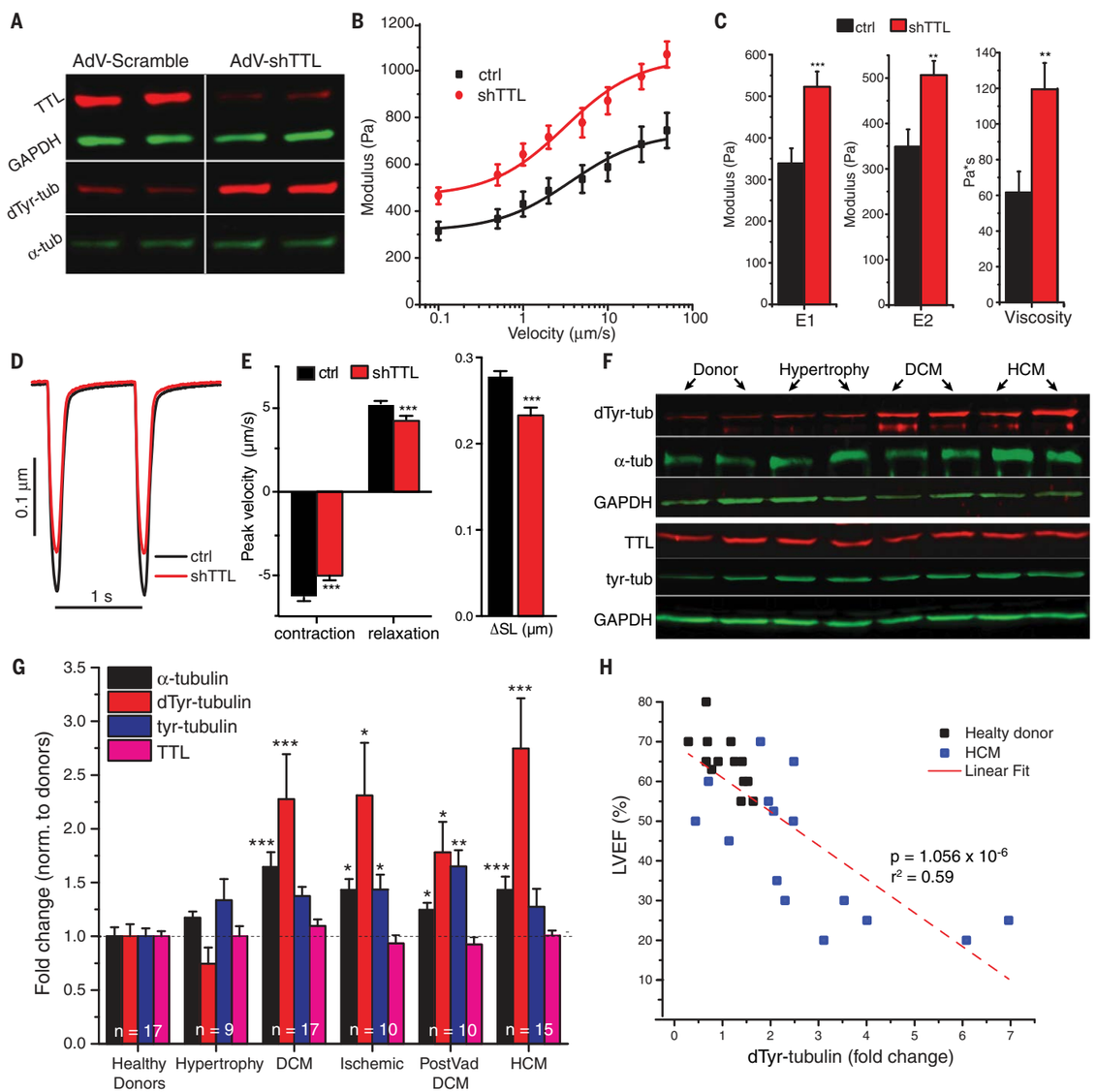

Fig. 7. Increasing detyrosination impairs contraction and is associated with human heart failure. (**A**) Western blot shows that shRNA against TTL selectively increases dTyr-tubulin without changing overall levels of α-tubulin. (**B**) Elastic modulus of control and shTTL-expressing myocytes at various indentation rates. (**C**) shTTL myocytes demonstrate increases in E1, E2, and viscosity. (**D** and **E**) TTL suppression significantly reduces contractile magnitude and velocity. (**F**) Representative Western blots from human heart lysates. (**G**) Data from pooled analysis; n = 17 healthy donors, 9 hypertrophy, 17 DCM, 11 ischemic, 10 with DCM following ventricular assist device support (VAD DCM), and 15 HCM hearts. (**H**) There was a negative correlation between LVEF and dTyr-tubulin expression in control and hypertrophic cardiomyopathy patients. Data are presented as means ± SEM; *P < 0.05, **P < 0.01, ***P < 0.001. Further statistical details are available in tables S7 to S9.

identity of TCP is unknown, it is unclear if upregulation of the detyrosinating enzyme may underlie this effect.

Discussion

Our findings demonstrate a regulatory pathway for MT load–bearing and myocyte mechanics through posttranslational detyrosination of tubulin. Detyrosinated MTs buckle under load in contracting cardiomyocytes, which confers mechanical resistance to contraction and regulating the viscoelastic properties of the myocyte.

The observation that MTs normally buckle, rather than break or slide, strongly indicates that they bear load and store elastic bending energy during the cardiac contractile cycle. This has implications for MT-dependent mechano-signaling in muscle and other tissues (*1*, *32*, *33*) but also has direct implications for contractility. Our model of myocyte contractility demonstrates how changing MT load–bearing and force transfer with the sarcomeres can substantially alter contractile properties. Our experimental data show that such changes in MT load–bearing can be achieved by posttranslational modifications of the MTs themselves, particularly detyrosination. The measured reductions in buckling and viscoelasticity and the increase in contractile speed of PTL-treated, TTL-overexpressing myocytes can all be attributed to changing the way MTs interact with the sarcomere and impairing their ability to act as compression resistors. It is also possible that detyrosinated MTs anchored to one sarcomere form bundles with MTs anchored to adjacent sarcomeres. If so, disrupting bundling would also effectively uncouple MTs from force-generating structures. Regardless of the mechanism, disrupting coupling to sarcomeres would reduce the incident force on the MT, and buckling occurrence would drop.

The striking periodicity of buckles in untreated myocytes lends further support to the idea of a sarcomeric anchor. The preferential association of desmin with detyrosinated tubulin and the insensitivity of desmin KO animals to changes in detyrosination strongly implicates desmin as at least one component of a sarcomeric anchoring complex of detyrosinated MTs. Note that myocytes lacking desmin have decreased viscoelasticity, despite a denser MT network, which supports the idea that MT network organization and cross-linking is a stronger determinant of myocyte mechanical properties than network density per se. Both the desmin and MT networks have elements perpendicular to their typical orientation, particularly near the sarcolemma, which may alter how those elements interact with the cytoskeleton and plasma membrane. However, we believe that the preponderance of the contractile resistance that results from detyrosination is due to longitudinal MTs in an orthogonal grid with transverse desmin IFs because of the simple numerical majority of cytoskeletal elements in this configuration.

Despite the fact that detyrosinated MTs store energy during sarcomere contraction, which provides compression resistance, little of this energy appears to return in the form of a restoring force that would quicken sarcomere extension. This implies that energy used to deform MTs undergoes substantial loss. Buckling of the MT exerts compressive force on the surrounding matrix and deforms the cytoplasm, which, due to its intrinsic viscosity, can act as an energy sink during each cycle. This is reflected in the large viscous component of the MT contributions to myocyte mechanical properties observed at deformation rates consistent with contractile velocities both in this and previous work (*34*). However, we do note a slight prolongation of the late phase of relaxation in TTL-overexpressing myocytes, which may represent the loss of a MT contribution to restoring force. We consider it probable that the restoring force of other internal elastic elements, such as titin, are likely to play a more dominant role, at least in the initial return toward resting sarcomere length (*27*). Thus, an increase in detyrosination may increase myocyte stiffness and impair contraction by acting as an energy sink, without providing significant energetic return during relaxation.

Consistent with this, an increase in detyrosination was associated with clinical contractile dysfunction in human hearts. Our cellular studies demonstrate that acute reduction of detyrosination with genetic or pharmacologic approaches can boost contractility and reduce mechanical stiffness. Additionally, these approaches are able to induce large changes in detyrosination, while only slightly altering the overall MT cytoskeleton, which minimizes off-target consequences. Thus, interfering with detyrosination may represent an attractive and novel therapeutic strategy for increasing contractility.

In conclusion, our data show that MTs exhibit divergent mechanical behavior because of the differences in how they couple to the rest of the cardiac cytoskeleton. The tyrosinated portions of the network, moving readily with the myocyte during contraction, provide little contractile resistance. Conversely, the detyrosinated portions of the MT network, forming complexes with desmin IFs, produce a cross-linked MT-IF network that confers robust resistance to contraction. This orthogonal MT-IF grid requires tightly periodic MT deformations to accommodate myocyte morphology changes during contraction. These deformations require a considerable amount of energy to form and dissipate a large fraction of that energy due to viscous interactions. This has important implications for MT load–bearing across cell biology, as well as for the altered mechanical stiffness and mechano-signaling in cardiac disease.

REFERENCES AND NOTES

1. B. L. Prosser, C. W. Ward, W. J. Lederer, *Science* **333**, 1440–1445 (2011).
2. B. L. Prosser, C. W. Ward, W. J. Lederer, *Cardiovasc. Res.* **98**, 307–314 (2013).
3. M. R. Zile *et al.*, *Circulation* **98**, 567–579 (1998).
4. S. Nishimura *et al.*, *Circ. Res.* **98**, 81–87 (2006).
5. H. L. Granzier, T. C. Irving, *Biophys. J.* **68**, 1027–1044 (1995).
6. C. P. Brangwynne *et al.*, *J. Cell Biol.* **173**, 733–741 (2006).
7. M. Mehrbod, M. R. K. Mofrad, *PLOS ONE* **6**, e25627 (2011).
8. H. Tsutsui, K. Ishihara, G. Cooper 4th, *Science* **260**, 682–687 (1993).
9. M. R. Zile *et al.*, *J. Am. Coll. Cardiol.* **33**, 250–260 (1999).
10. G. Cooper 4th, *Am. J. Physiol. Heart Circ. Physiol.* **291**, H1003–H1014 (2006).
11. C. Janke, J. C. Bulinski, *Nat. Rev. Mol. Cell Biol.* **12**, 773–786 (2011).
12. J. P. Kerr *et al.*, *Nat. Commun.* **6**, 8526 (2015).
13. H. Sato *et al.*, *J. Cell Biol.* **139**, 963–973 (1997).
14. S. Belmadani, C. Poüs, R. Ventura-Clapier, R. Fischmeister, P.-F. Méry, *Mol. Cell. Biochem.* **237**, 39–46 (2002).
15. E. White, *Pflugers Arch.* **462**, 177–184 (2011).
16. G. Cooper 4th, *Heart Fail. Rev.* **5**, 187–201 (2000).
17. L. Cassimeris, P. Tran, *Methods Cell Biol.* **97**, xvii–xviii (2010).
18. G. Lukinavičius *et al.*, *Nat. Methods* **11**, 731–733 (2014).
19. S. Belmadani, C. Poüs, R. Fischmeister, P.-F. Méry, *Mol. Cell. Biochem.* **258**, 35–48 (2004).
20. C. Janke *et al.*, *Science* **308**, 1758–1762 (2005).
21. C. Erck *et al.*, *Proc. Natl. Acad. Sci. U.S.A.* **102**, 7853–7858 (2005).
22. L. Peris *et al.*, *J. Cell Biol.* **185**, 1159–1166 (2009).
23. M. Sirajuddin, L. M. Rice, R. D. Vale, *Nat. Cell Biol.* **16**, 335–344 (2014).
24. G. Kreitzer, G. Liao, G. G. Gundersen, *Mol. Biol. Cell* **10**, 1105–1118 (1999).
25. R. A. Whipple *et al.*, *Cancer Res.* **68**, 5678–5688 (2008).
26. X. Fonrose *et al.*, *Cancer Res.* **67**, 3371–3378 (2007).
27. M. Helmes, K. Trombitás, H. Granzier, *Circ. Res.* **79**, 619–626 (1996).
28. R. E. Mahaffy, C. K. Shih, F. C. MacKintosh, J. Käs, *Phys. Rev. Lett.* **85**, 880–883 (2000).
29. P. Konieczny *et al.*, *J. Cell Biol.* **181**, 667–681 (2008).
30. G. Liao, G. G. Gundersen, *J. Biol. Chem.* **273**, 9797–9803 (1998).
31. G. Gurland, G. G. Gundersen, *J. Cell Biol.* **131**, 1275–1290 (1995).
32. R. J. Khairallah *et al.*, *Sci. Signal.* **5**, ra56 (2012).
33. M. Prager-Khoutorsky, A. Khoutorsky, C. W. Bourque, *Neuron* **83**, 866–878 (2014).
34. H. Tagawa *et al.*, *Circ. Res.* **80**, 281–289 (1997).

ACKNOWLEDGMENTS

The authors thank C. W. Ward and E. L. Holzbaur for kindly providing TTL and EMTB-3xGFP plasmids, respectively, as well as for discussion; R. Bloch for providing desmin KO mice and littermate controls; Carl Zeiss Microscopy for Airyscan instrumentation use; IonOptix for technical support and cell holder materials; and Y. E. Goldman, E. L. Grishchuk, and R. J. Composto for discussion and guidance. B.L.P., P.R., M.A.C., A.I.B., and K.B.M. were responsible for experimental design; B.L.P., P.R., M.A.C., C.Y.C., and A.I.B. carried out experiments and analyzed data; H.A. and V.B.S. designed and executed the mathematical model. B.L.P. and P.R. cowrote the manuscript. All authors participated in the critical review and revision of the manuscript. This work was supported by funding from National Institute for Arthritis and Musculoskeletal and Skin Diseases (NIH) (T32AR053461-09 to P.R. and T32HL007954 to M.A.C.) and from National Heart, Lung, and Blood Institute (NIH) (R00-HL114879 to B.L.P.). The VIVA experiments used shared experimental facilities from the Nano Science and Engineering Center on Molecular Function at the Nano-Bio Interface at the University of Pennsylvania supported by NSF under grant DMR08-32802. We thank R. Composto, who acknowledges the NSF Polymers Program under grant DMR09-07493. Procurement of human heart tissue was enabled by grants from NIH (HL089847 and HL105993) to K.B.M. H.A. and V.B.S. are supported by the National Institute of Biomedical Imaging and Bioengineering (NIH) under award number R01EB017753 and NSF grant CMMI-1312392. The data are included in the main manuscript and in the supplementary materials online.

SUPPLEMENTARY MATERIALS

www.sciencemag.org/content/352/6284/aaf0659/suppl/DC1
Materials and Methods
Supplementary Text
Figs. S1 to S11
Tables S1 to S9
References (35–42)
Movies S1 to S8

12 December 2015; accepted 29 January 2016
10.1126/science.aaf0659

NEURODEVELOPMENT

Complement and microglia mediate early synapse loss in Alzheimer mouse models

Soyon Hong,[1] Victoria F. Beja-Glasser,[1]* Bianca M. Nfonoyim,[1]* Arnaud Frouin,[1] Shaomin Li,[2] Saranya Ramakrishnan,[1] Katherine M. Merry,[1] Qiaoqiao Shi,[2] Arnon Rosenthal,[3,4,5] Ben A. Barres,[6] Cynthia A. Lemere,[2] Dennis J. Selkoe,[2,7] Beth Stevens[1,8]†

Synapse loss in Alzheimer's disease (AD) correlates with cognitive decline. Involvement of microglia and complement in AD has been attributed to neuroinflammation, prominent late in disease. Here we show in mouse models that complement and microglia mediate synaptic loss early in AD. C1q, the initiating protein of the classical complement cascade, is increased and associated with synapses before overt plaque deposition. Inhibition of C1q, C3, or the microglial complement receptor CR3 reduces the number of phagocytic microglia, as well as the extent of early synapse loss. C1q is necessary for the toxic effects of soluble β-amyloid (Aβ) oligomers on synapses and hippocampal long-term potentiation. Finally, microglia in adult brains engulf synaptic material in a CR3-dependent process when exposed to soluble Aβ oligomers. Together, these findings suggest that the complement-dependent pathway and microglia that prune excess synapses in development are inappropriately activated and mediate synapse loss in AD.

Genome-wide association studies implicate microglia and complement-related pathways in Alzheimer's disease (AD) (*1*). Previous research has demonstrated both beneficial and detrimental roles of complement and microglia in plaque-related neuropathology (*2*, *3*); however, their roles in synapse loss, a major pathological correlate of cognitive decline in AD (*4*), remain to be identified. Emerging research implicates microglia and immune-related mechanisms in brain wiring in the healthy brain (*1*). During development, C1q and C3 localize to synapses and mediate synapse elimination by phagocytic microglia (*5*–*7*). We hypothesized that this normal developmental synaptic pruning pathway is activated early in the AD brain and mediates synapse loss.

The degree of region-specific synapse loss is a stronger correlate of cognitive decline in AD than counts of plaques, tangles, and neuronal loss (*8*, *9*). To determine how early synapse loss occurs, we used superresolution structured illumination microscopy (SIM) (*10*) to quantify synapse density in hippocampal CA1 stratum radiatum of familial AD-mutant human amyloid precursor protein (hAPP) ("J20") transgenic mice (*11*). Quantification of colocalized pre- and postsynaptic puncta [synaptophysin and postsynaptic density 95 (PSD95) (Fig. 1A); synaptotagmin and homer (fig. S1, A to D)] revealed a significant loss of synapses in J20 hippocampus at 3 to 4 months old (mo), an age that precedes plaque deposition (*11*, *12*). Synapse loss in preplaque J20 CA1 was confirmed by electron microscopy (fig. S1G). Confocal imaging also showed synapse loss in CA1, CA3, and dentate gyrus of 3 mo J20 hippocampus but not in striatum (fig. S1E). Synapse levels were not altered in 1 mo J20 brains versus wild type (WT) littermates (fig. S1F), suggesting that the hippocampal synaptic loss at 3 mo is likely not a result of abnormal synaptic development.

We asked whether the classical complement cascade is up-regulated in preplaque brains when synapses are already vulnerable. C1q immunoreactivity (*13*) (antibody now available at Abcam) was elevated in J20 brains as early as 1 mo and preceding synapse loss (Fig. 1B and fig. S1). C1q elevation was region-specific, particularly in the hippocampus and frontal cortex, two regions vulnerable to synapse loss (*14*) (Fig. 1B and fig. S2A). C1q immunoreactivity was comparable between J20 and WT mice at postnatal day 21 (P21) (fig. S2B), suggesting that elevated levels at 1 mo are likely not a developmental artifact. C1q was also similarly increased in the hippocampus of another model of AD, the APP/PS1 (presenilin 1) mice (*15*) (fig. S2C). Notably, SIM demonstrated colocalization of C1q with PSD95-positive puncta in 1 mo J20 hippocampus (Fig. 1C). A higher percentage of PSD95 colocalized with C1q in the hippocampus of J20 mice than in that of WT littermates (Fig. 1D and fig. S3), suggesting that the C1q-associated synapses may be marked for elimination.

Punctate Aβ was found deposited in J20 hippocampus at 1 mo (fig. S4), long before Aβ plaques deposit (*11*, *12*), raising the question of whether C1q increase in these preplaque brains is dependent on soluble Aβ levels. To test this hypothesis, we injected the mice with compound E, a γ-secretase inhibitor that rapidly decreases Aβ production (*12*). Compound E markedly reduced soluble Aβ levels in J20 mice; there was a corresponding reduction of C1q deposition (Fig. 1E), suggesting that Aβ upregulates C1q. To further address whether the increase of C1q is dependent on soluble Aβ, and if so, which species, we injected soluble Aβ oligomers or monomers into lateral ventricles of WT mice. Hippocampus contralateral to the injection site was examined to avoid any surgery-related effects. Oligomeric Aβ (oAβ), which is prefibrillar in nature and acts as a mediator of synapse loss and dysfunction in AD (*4*), but not the relatively innocuous monomeric Aβ or vehicle, induced C1q deposition (Fig. 2A and fig. S5). A higher percentage of PSD95 colocalized with C1q in oAβ-injected versus monomer-injected mice (Fig. 2B), in a manner similar to this colocalization in J20 mice. Together, these findings show an early and aberrant increase and synaptic localization of C1q in multiple AD model systems. Furthermore, fluorescent in situ hybridization (FISH) demonstrated up-regulated *C1qa* expression in microglia (fig. S6), implicating microglia as a major source of C1q in these preplaque brains.

To test whether C1q and oAβ act in a common pathway to eliminate synapses, we injected oAβ into lateral ventricles of *C1qa* knockout (KO) mice (*16*). Soluble oAβ induced a significant loss of colocalized synapsin- and PSD95-immunoreactive puncta in WT mice within 72 hours (Fig. 3A, left panel) (*17*). In contrast, oAβ failed to induce synapse loss in *C1qa* KO mice (Fig. 3A, right panel), suggesting that C1q is required for oAβ-induced synapse loss in vivo. To determine whether local, acute inhibition of C1 activation could similarly blunt the synaptotoxic effects of oAβ, we used an antibody against C1q (anti-C1q) (ANX-M1, Annexon Biosciences), which blocks the classical complement cascade (see fig. S7

[1]F.M. Kirby Neurobiology Center, Boston Children's Hospital (BCH) and Harvard Medical School (HMS), Boston, MA 02115, USA. [2]Ann Romney Center for Neurologic Diseases, Department of Neurology, Brigham and Women's Hospital (BWH) and HMS, Boston, MA 02115, USA. [3]Alector Inc., 953 Indiana Street, San Francisco, CA 94107, USA. [4]Annexon Biosciences, 280 Utah Avenue Suite 110, South San Francisco, CA 94080, USA. [5]Department of Anatomy, University of California San Francisco (UCSF), San Francisco, CA 94143, USA. [6]Department of Neurobiology, Stanford University School of Medicine, Palo Alto, CA 94305, USA. [7]Prothena Biosciences, Dublin, Ireland. [8]Stanley Center for Psychiatric Research, Broad Institute of MIT and Harvard, Cambridge, MA 02142, USA.
*These authors contributed equally to this work. **†Corresponding author. Email: beth.stevens@childrens.harvard.edu**

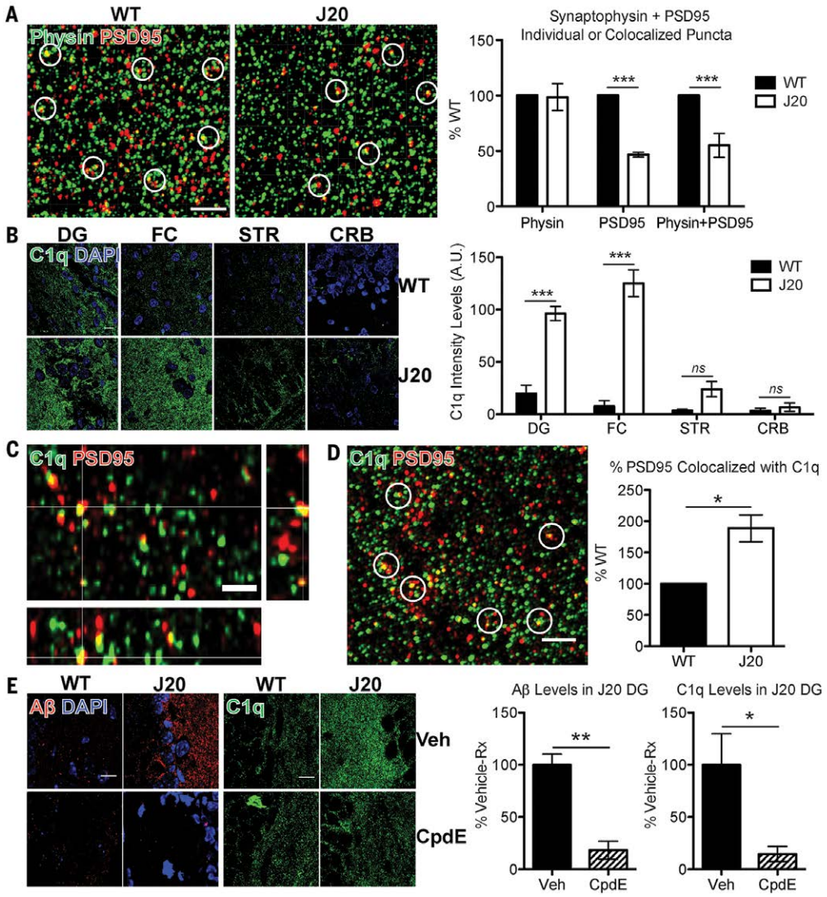

Fig. 1. C1q up-regulation and deposition onto synapses precede pre-plaque synapse loss in J20 mice. (**A**) Superresolution SIM images of synaptophysin (green)– and PSD95 (red)–immunoreactive puncta in stratum radiatum of 3 mo J20 or WT hippocampus (CA1). Quantification of synaptic puncta or their apposition using Imaris indicates selective loss of PSD95 in J20 hippocampus as compared to their WT littermate controls. See fig. S1. (**B**) Region-specific up-regulation of C1q (green) in 1 mo J20; DG, dentate gyrus; FC, frontal cortex; STR, striatum; CRB, cerebellum; DAPI, 4′,6-diamidino-2-phenylindole. See fig. S2. (**C**) Orthogonal view of SIM image showing colocalization of C1q (green) and PSD95 (red). (**D**) Higher percentage of PSD95 colocalized with C1q in 1 mo J20 dentate gyrus versus WT. (**E**) Compound E reduces deposited soluble Aβ (red) and C1q (green) in 1 mo J20 dentate gyrus, with minimal effect on C1q levels in WT mice. Scale bar, 2 μm (A, C, and D) or 10 μm (B and E). Means ± SEM; $n = 3$ or 4 mice per genotype or per treatment group per genotype. $^{*}P < 0.05$, $^{**}P < 0.01$, or $^{***}P < 0.001$ using two-way analysis of variance (ANOVA) followed by Bonferroni posttest (A and B), two-tailed one-sample t test (D), or two-tailed unpaired t test (E).

and supplementary methods). Coadministration of the ANX-M1 anti-C1q antibody, but not its immunoglobulin G (IgG) isotype control, prevented oAβ from inducing synapse loss in WT mice (Fig. 3B). Thus, blocking C1 activation by either genetic or antibody-mediated means lessened oAβ's synaptotoxic effects.

To determine whether C1q is associated with synaptic dysfunction, we asked whether the established ability of oAβ to potently inhibit long-term potentiation (LTP) (*4*) was dependent on C1q. We tested the functional effects of the ANX-M1 anti-C1q antibody in acute hippocampal slices treated with oAβ. IgG alone had negligible effects on LTP induction in WT mouse hippocampal slices and on the ability of oAβ to inhibit LTP; however, pretreatment of hippocampal slices with the anti-C1q antibody significantly prevented the impairment of LTP by oAβ (Fig. 3C). Neither ANX-M1 nor its IgG control altered basal synaptic neurotransmission (fig. S8). Collectively, these results in hippocampal slices and in mice support C1q as a key mediator of oAβ-induced synaptic loss and dysfunction.

In the healthy developing brain, C1q promotes activation of C3, which opsonizes subsets of synapses for elimination, a process that is down-regulated in the mature brain (*5*, *6*). However, oAβ induced a significant C3 deposition in WT adult mice (fig. S7A, upper panel). This was significantly reduced in both the *C1qa* KO (fig. S7A, lower panel) and the ANX-M1 anti-C1q antibody–treated WT mice (fig. S7B), suggesting that the C3

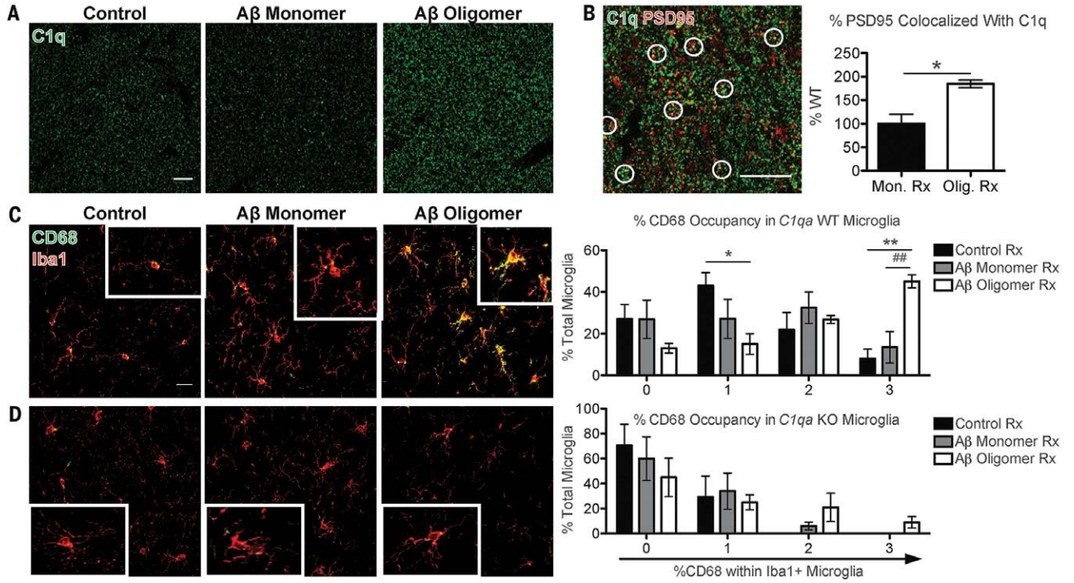

Fig. 2. Oligomeric Aβ increases C1q and microglial phagocytic activity. (**A** and **B**) Soluble Aβ oligomers in WT mice led to elevation of C1q (green) (A) and a higher percentage of PSD95 (red) colocalization with C1q versus monomers (B). (**C** and **D**) oAβ induced high levels of CD68 (green) immunoreactivity in Iba1-positive (red) microglia in WT mice (C), but not in those of *C1qa* KO mice (D). Both had negligible changes in morphology. See fig. S10. Scale bar, 10 μm (A), 5 μm (B), or 20 μm (C). Means ± SEM; $n = 3$ to 5 mice per treatment group per genotype. $^{*}P < 0.05$ using two-tailed t test (B) or $^{*}P < 0.05$, $^{**}P < 0.01$ versus control-treated or $^{\#\#}P < 0.01$ versus Aβ monomer–treated using two-way ANOVA followed by Bonferroni posttest (C).

Fig. 3. Complement is necessary for synapse loss and dysfunction in AD models. (**A**) Aβ oligomers induced loss of colocalized synapsin- and PSD95-immunoreactive puncta in the contralateral hippocampus of 3 mo WT mice (left panel); however, they failed to do so in *C1qa* KO mice (right panel). (**B**) Coinjection of Aβ oligomers with the function-blocking antibody against C1q, ANX-M1, but not with its IgG isotype control, prevented synapse loss in WT mice. (**C**) Pretreatment of hippocampal slices with the anti-C1q antibody, ANX-M1, prevented Aβ-mediated LTP inhibition (green) versus IgG (red). IgG alone had a minimal effect (blue) versus artificial cerebrospinal fluid (aCSF) vehicle (black). $n = 6$ to 11 slices per group. (**D**) Percentage of PSD95 co-localized with C3 is increased in APP/PS1 hippocampus versus that of WT mice. (**E** and **F**) Genetic deletion of *C3* prevents synapse loss in 4 mo APP/PS1 mice. Quantification of colocalized immunoreactive puncta for synaptotagmin and homer in dentate gyrus (E) or synaptophysin and PSD95 in CA1 stratum radiatum (F) of WT, APP/PS1, APP/PS1x*C3* KO, and *C3* KO hippocampi. Means ± SEM; $n = 3$ to 5 mice per genotype or per treatment group per genotype. $^{*}P < 0.05$, $^{**}P < 0.01$, or $^{***}P < 0.001$ using two-tailed one-sample t test (D), one-way (A, C, E, F) or two-way (B) ANOVA followed by Bonferroni posttest. ns, not significant.

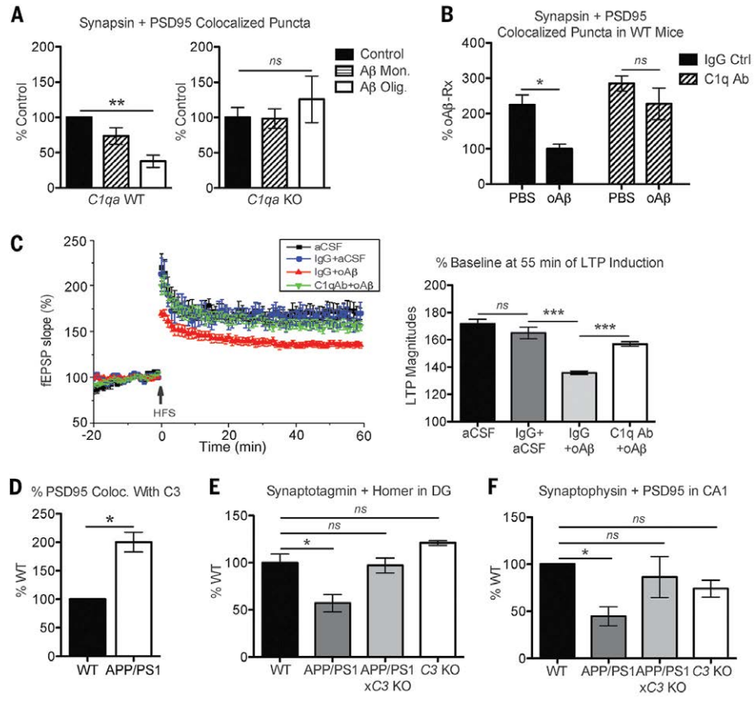

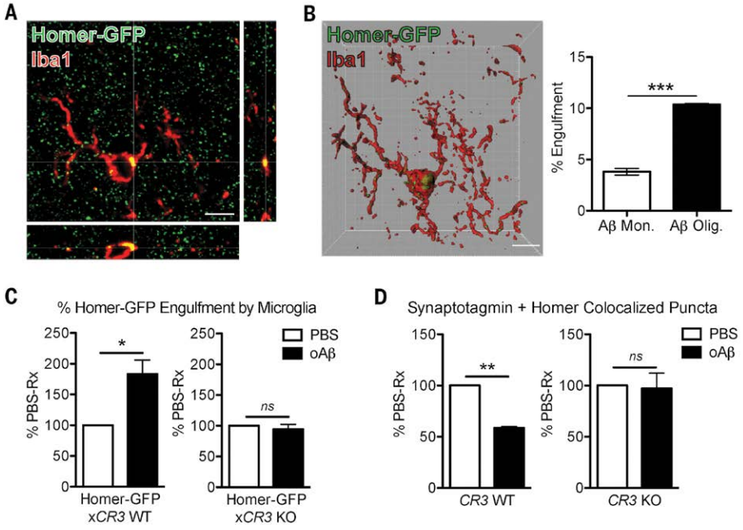

Fig. 4. Microglia engulf synapses via CR3 upon oligomeric Aβ challenge. (**A**) Orthogonal view of high-resolution confocal image shows colocalization of homer-GFP and Iba1 (red). (**B**) Three-dimensional reconstruction and surface rendering using Imaris demonstrate larger volumes of homer-GFP puncta inside microglia of oAβ-injected contralateral hippocampus versus those of monomer-injected. (**C**) Microglia of homer-GFPx*CR3* KO mice (right panel) show less engulfment of homer-GFP when challenged with oAβ versus those of homer-GFP mice (left panel). (**D**) Aβ oligomers failed to induce synapse loss in the contralateral hippocampus of *CR3* KO mice (right panel) as they did in WT mice (left panel). Scale bar, 5 μm (A and B). Means ± SEM; *n* = 3 mice per treatment group per genotype (*n* = 6 to 17 microglia analyzed per mouse). **P* < 0.05, ***P* < 0.01, or ****P* < 0.0001 using two-tailed *t* test (B) or two-tailed one-sample *t* test (C and D). ns, not significant.

deposition in this model is downstream of the classical complement cascade. Consistent with these findings, a higher percentage of PSD95 colocalized with C3 in J20 and APP/PS1 brains (Fig. 3D and fig. S9). To determine whether C3 is necessary for early synapse loss in AD genetic models, we crossed APP/PS1 mice, which, similar to the J20 mice, had a significant increase and localization of C1q and C3 onto hippocampal synapses (figs. S2C and S9), to *C3*-deficient mice (*18*). Quantification of colocalized pre- and post-synaptic puncta demonstrated synapse loss in 4 mo APP/PS1 hippocampus as compared to WT; however, APP/PS1x*C3* KO mice did not display this synapse loss (Fig. 3, E and F). Together, our data indicate that genetic deletion of *C3* ameliorates synapse loss in APP/PS1 mice, providing further evidence that the classical complement cascade mediates early synapse loss in AD mouse models.

Microglia express complement receptors and mediate synaptic pruning in the developing brain (*1*, *6*), raising the question of whether this normal developmental pruning pathway could be activated to mediate synapse loss in the preplaque AD brain. Consistent with this hypothesis, microglia had increased amounts of the lysosomal protein CD68 in J20 hippocampus compared to WT and less so in striatum, a less vulnerable region (figs. S1C and S10). Furthermore, in WT mice challenged with oAβ, microglia had significantly increased levels of CD68 immuno-reactivity (Fig. 2C). However, in *C1qa* KO mice in which synapse loss was rescued, oAβ failed to induce such an increase (Fig. 2D), suggesting that microglia eliminate synapses through the complement pathway.

To directly test whether phagocytic microglia engulf synaptic elements, we adapted our in vivo synaptic engulfment assay (*19*) using intracerebroventricular injections of Aβ in homer-GFP (green fluorescent protein) mice (*20*) (Fig. 4A). oAβ induced a significantly higher volume of internalized homer-GFP in microglia than monomeric Aβ controls did at the contralateral hippocampus (Fig. 4B), indicating that microglia engulf synaptic elements when challenged with oAβ. Internalized homer-GFP often colocalized with CD68 (fig. S11A), suggesting that the engulfed synapses are internalized into lysosomal compartments in a manner similar to that of developmental synaptic pruning (*6*). Notably, oAβ failed to increase synaptic engulfment in microglia lacking CR3 (*21*), a high-affinity receptor for C3 expressed on macrophages [homer-GFPx*CR3* KO versus homer-GFP mice, which received tail vein injections of phosphate-buffered saline (PBS) or oAβ (Fig. 4C)]. These data demonstrate that CR3 is necessary for oAβ-dependent engulfment of synapses by microglia.

To test whether inhibition in microglial engulfment leads to protection against oAβ-induced synapse loss, we performed tail vein injections of oAβ into WT and *CR3* KO mice. oAβ induced synapse loss in the hippocampus of WT mice but not in that of *CR3* KO mice (Fig. 4D). All CR3-positive microglia were P2RY12-positive (fig. S11), indicating that they are resident cells (*22*). Altogether, these results suggest that resident microglia engulf synaptic material when challenged by oAβ through a complement-dependent mechanism.

Synaptic deficits occur in early AD and mild cognitive impairment before onset of plaques and are some of the first signs of the neuronal degenerative process (*4*, *23*–*25*). Here we identify critical synaptotoxic roles of complement and microglia in AD models before plaque formation and neuroinflammation, in regions of the hippocampus undergoing synapse loss. Using multiple experimental approaches, we demonstrate a region-specific increase of phagocytic microglia and accumulation of C1q and C3 on synapses in preplaque brains. Microglia in the adult brain, when challenged with synaptotoxic, soluble Aβ oligomers, engulf synapses in the absence of plaque aggregates; deletion of CR3 blocks this process. Finally, inhibiting C1q, C3, or CR3 activity rescues synaptic loss and dysfunction.

Our data suggest a local activation of a developmental pruning pathway (*5*, *6*) as a key mechanism underlying oAβ-induced synapse loss in preplaque AD brain. C1q is aberrantly increased by diffusible oAβ in a region-specific manner and deposits onto synapses, triggering the activation of downstream classical complement pathway and phagocytic microglia. Blocking Aβ production in J20 mice significantly ameliorated C1q deposition in the hippocampus, and genetic or antibody-mediated inhibition of complement blocks oAβ from inducing microglial synaptic engulfment, synapse loss, and LTP inhibition. These complementary findings have direct therapeutic relevance.

We propose a model in which C1q and oAβ operate in a common pathway to activate the complement cascade and drive synapse elimination by microglia through CR3 (fig. S12). This could occur in multiple ways: Soluble oAβ associates with synaptic membranes and other synaptic markers (*4*, *26*); thus, oAβ bound to synapses may anchor C1q directly. Alternatively, oAβ binding to synapses may weaken the synapse (*4*) and expose a C1q receptor. Although specific receptors for C1q at synapses are not yet known, we have shown that C1q binds synapses in vulnerable regions undergoing synapse loss (*5*, *27*). It is also plausible that oAβ and C1q may work indirectly to mediate synapse loss through cytokines such as transforming growth factor–β (*7*), through microglial or astrocytic activation, or through other mechanisms, including major histocompatibility complex class I (MHCI)–PirB, another immune pathway critical for synapse elimination in development and AD (*28*–*30*).

Finally, our studies show that resident microglia in the adult central nervous system phagocytose synapses when challenged by synaptotoxic oAβ, implicating microglia as potential cellular mediators of synapse loss. Although microglia and complement activation are prominently involved in plaque maintenance and related periplaque neuropathology, their roles have heretofore been largely regarded as a secondary event related to neuroinflammation (*2*). Our studies directly challenge this view and suggest that microglia and immune-related pathways can act as early mediators of synapse loss and dysfunction that occur in AD models before plaques form. Although the complement pathway may not be involved in all pathological routes to AD, including plaque-associated synapse loss, the work reported here provides new insights into how synapses are lost in AD. It will be important in future studies to examine whether this microglia or the complement-dependent pathway also plays a role in plaque-associated synapse loss or in other synaptopathies, including tauopathies and Huntington's disease. If so, our findings may suggest complement and microglia as potential early therapeutic targets in AD and other neurodegenerative diseases involving synaptic dysfunction and memory decline.

REFERENCES AND NOTES

1. S. Hong, L. Dissing-Olesen, B. Stevens, *Curr. Opin. Neurobiol.* **36**, 128–134 (2016).
2. T. Wyss-Coray, J. Rogers, *Cold Spring Harb. Perspect. Med.* **2**, l a006346 (2012).
3. M. E. Benoit *et al.*, *J. Biol. Chem.* **288**, 654–665 (2013).
4. L. Mucke, D. J. Selkoe, *Cold Spring Harb. Perspect. Med.* **2**, a006338 (2012).
5. B. Stevens *et al.*, *Cell* **131**, 1164–1178 (2007).
6. D. P. Schafer *et al.*, *Neuron* **74**, 691–705 (2012).
7. A. R. Bialas, B. Stevens, *Nat. Neurosci.* **16**, 1773–1782 (2013).
8. S. T. DeKosky, S. W. Scheff, *Ann. Neurol.* **27**, 457–464 (1990).
9. R. D. Terry *et al.*, *Ann. Neurol.* **30**, 572–580 (1991).
10. S. Hong, D. Wilton, B. Stevens, D. S. Richardson, Structured Illumination Microscopy for the Investigation of Synaptic Structure and Function. In *Methods in Molecular Biology; Synapse Development: Methods and Protocols*.
11. L. Mucke *et al.*, *J. Neurosci.* **20**, 4050–4058 (2000).
12. S. Hong *et al.*, *J. Neurosci.* **31**, 15861–15869 (2011).
13. A. H. Stephan *et al.*, *J. Neurosci.* **33**, 13460–13474 (2013).
14. J. A. Harris *et al.*, *J. Neurosci.* **30**, 372–381 (2010).
15. J. L. Jankowsky *et al.*, *Hum. Mol. Genet.* **13**, 159–170 (2004).
16. M. Botto *et al.*, *Nat. Genet.* **19**, 56–59 (1998).
17. D. B. Freir *et al.*, *Neurobiol. Aging* **32**, 2211–2218 (2011).
18. M. R. Wessels *et al.*, *Proc. Natl. Acad. Sci. U.S.A.* **92**, 11490–11494 (1995).
19. D. P. Schafer, E. K. Lehrman, C. T. Heller, B. Stevens, *J. Vis. Exp.* **88**, 51482 (2014).
20. T. Ebihara, I. Kawabata, S. Usui, K. Sobue, S. Okabe, *J. Neurosci.* **23**, 2170–2181 (2003).
21. A. Coxon *et al.*, *Immunity* **5**, 653–666 (1996).
22. O. Butovsky *et al.*, *Nat. Neurosci.* **17**, 131–143 (2014).
23. D. J. Selkoe, *Science* **298**, 789–791 (2002).
24. S. W. Scheff, D. A. Price, F. A. Schmitt, E. J. Mufson, *Neurobiol. Aging* **27**, 1372–1384 (2006).
25. S. W. Scheff, D. A. Price, F. A. Schmitt, S. T. DeKosky, E. J. Mufson, *Neurology* **68**, 1501–1508 (2007).
26. S. Hong *et al.*, *Neuron* **82**, 308–319 (2014).
27. A. H. Stephan, B. A. Barres, B. Stevens, *Annu. Rev. Neurosci.* **35**, 369–389 (2012).
28. A. Datwani *et al.*, *Neuron* **64**, 463–470 (2009).
29. T. Kim *et al.*, *Science* **341**, 1399–1404 (2013).
30. H. Lee *et al.*, *Nature* **509**, 195–200 (2014).

ACKNOWLEDGMENTS

We thank B. Sabatini (HMS), T. Bartels (BWH), and members of the Stevens laboratory for critical reading of the manuscript; L. Dissing-Olesen (BCH) for help with the conceptual figure (fig. S12), M. Ericsson [HMS electron microscopy (EM) facility] for EM imaging, K. Kapur (BCH) for advice on statistics, D. M. Walsh (BWH) for Ab oligomers (S26C), S. Okabe (University of Tokyo) for homer-GFP mice, and M. Leviten and T. Yednock (Annexon Biosciences) for characterization and advice on the ANX-M1 anti-C1q antibody; D. Richardson (Harvard Center for Biological Imaging), A. Hill BCH Intellectual and Developmental Disabilities Research Center Cellular Imaging Core NIH-P30-HD-18655, and H. Elliot and T. Xie (HMS Image and Data Analysis Core) for assistance with imaging and data analysis; and S. Kim (BWH), K. Colodner (BCH), and S. Matousek (BWH) for assistance with mice. The J20 mice, *C1qa* KO mice, P2RY12 antibody, and the ANX-M1 C1q function-blocking antibody are available from L. Mucke, M. Botto, O. Butovsky, and A. Rosenthal under material transfer agreements with UCSF Gladstone, Imperial College London, BWH, and Annexon Biosciences, respectively. A.R. is a cofounder, consultant, and chairman of the board of directors; B.A.B. is a cofounder and chairman of the scientific advisory board; and B.S. serves on the scientific advisory board of Annexon LLC. A.R., B.A.B., and B.S. are minor shareholders of Annexon LLC. All other authors declare no competing financial interests related to this project. The following patents related to this project have been granted or applied for: PCT/2015/010288 (S.H. and B.S.), US14/988387 and EP14822330 (S.H., A.R., and B.S.), and US8148330, US9149444, US20150368324, US20150368325, US20150368326, and US20120328601 (B.S. and B.A.B.). This work was funded by an Edward R. and Anne G. Lefler Fellowship (S.H.), Coins for Alzheimer's Research Trust (B.S.), Fidelity Biosciences Research Initiative (F-Prime) (B.S. and C.A.L.), JPB Foundation (B.A.B.), the National Institutes of Health AG000222 (S.H.), National Institute of Neurological Disorders and Stroke–NIH R01NS083845 (D.J.S.), National Institute on Aging–NIH 1RF1AG051496A (B.S.). Supplementary materials contain additional data, including materials and methods. S.H. and B.S. designed the study and wrote the manuscript, with help from all authors. S.H. performed most experiments and data analysis; V.F.B.-G. and B.M.N. performed microglial activation and engulfment experiments along with immunohistochemistry; S.R. and K.M.M. performed C1q immunohistochemistry; A.F. performed FISH; S.L. performed electrophysiology; Q.S. and C.A.L. assisted with design and collection of APP/PS1 tissue; A.R. and B.A.B. designed and characterized the ANX-M1 antiC1q antibody; and D.J.S. contributed in the discussions and experimental design.

SUPPLEMENTARY MATERIALS

www.sciencemag.org/cgi/content/full/science.aad8373/DC1
Materials and Methods
Figs. S1 to S12

10 November 2015; accepted 18 March 2016
Published online 31 March 2016
10.1126/science.aad8373

BIOMEDICAL ENGINEERING

Bioengineering a 3D integumentary organ system from iPS cells using an in vivo transplantation model

Ryoji Takagi,[1*] Junko Ishimaru,[1*] Ayaka Sugawara,[1*] Koh-ei Toyoshima,[2,3,4] Kentaro Ishida,[5] Miho Ogawa,[2,3,4] Kei Sakakibara,[1] Kyosuke Asakawa,[2] Akitoshi Kashiwakura,[1] Masamitsu Oshima,[5] Ryohei Minamide,[2] Akio Sato,[4] Toshihiro Yoshitake,[4] Akira Takeda,[4] Hiroshi Egusa,[6] Takashi Tsuji[2,3,5†]

The integumentary organ system is a complex system that plays important roles in waterproofing, cushioning, protecting deeper tissues, excreting waste, and thermoregulation. We developed a novel in vivo transplantation model designated as a clustering-dependent embryoid body transplantation method and generated a bioengineered three-dimensional (3D) integumentary organ system, including appendage organs such as hair follicles and sebaceous glands, from induced pluripotent stem cells. This bioengineered 3D integumentary organ system was fully functional following transplantation into nude mice and could be properly connected to surrounding host tissues, such as the epidermis, arrector pili muscles, and nerve fibers, without tumorigenesis. The bioengineered hair follicles in the 3D integumentary organ system also showed proper hair eruption and hair cycles, including the rearrangement of follicular stem cells and their niches. Potential applications of the 3D integumentary organ system include an in vitro assay system, an animal model alternative, and a bioengineered organ replacement therapy.

INTRODUCTION

Organogenesis is a complex process involving tissue self-organization, cell-cell interactions, regulation of signaling molecules, and cell movement (*1*–*3*). Almost all organs arise from organ germs, which are induced by reciprocal epithelial-mesenchymal interactions in each organ-forming field (*4*). Current regenerative therapy uses tissue stem cell transplantation to restore damaged tissues and organs in a wide variety of diseases (*5*–*7*). Next-generation regenerative therapy consists of organ replacement regenerative therapy, which aims to reproduce the reciprocal epithelial-mesenchymal interactions during embryogenesis. This organ regeneration therapy represents a fundamental approach to treating patients who experience organ dysfunction as a result of disease, injury, or aging (*8*). Our recent studies provided the proof of concept that fully functional regeneration of ectodermal organs, such as teeth, hair follicles, and salivary and lachrymal glands, could be achieved with the transplantation of bioengineered organ germs using the organ germ method (*9*–*13*). However, organ-inductive stem cells in a wide variety of organs, except hair follicles, exist only during embryonic organogenesis (*2*). Thus, we must develop techniques to reconstitute a wide variety of bioengineered organ germs using pluripotent stem cells, such as embryonic stem (ES) cells and induced pluripotent stem (iPS) cells (*2*, *14*).

Pluripotent stem cells, such as ES and iPS cells, can be induced to differentiate into specific somatic cell lineages using cytokines that mimic the patterning and positioning signals during embryogenesis (*15*). In the embryo, patterning signals indicating body axis and organ-forming fields are strictly controlled by signaling centers according to the embryonic body plan (*16*). These complex pattern formation signals in local areas of the body may lack centralized organizing signals, as observed in the generation of teratomas, which include disorganized neural tissues, cartilage, muscle, and bronchial epithelia (*17*). Although it is difficult to control the development of specific types of compartmentalized tissues, several groups recently reported neuroectodermal and endodermal organs generated via the regulation of complex patterning signals during embryogenesis and self-formation of pluripotent stem cells in three-dimensional (3D) stem cell culture (*2*, *3*, *18*–*22*). However, ectodermal organs, such as the skin, hair follicles, teeth, and exocrine organs, have not been generated with sufficient reproducibility from pluripotent stem cells in 3D stem cell culture or by transplantation (*3*).

The integumentary organ system (IOS) is a complex system that plays important roles in waterproofing, cushioning, protecting deeper tissues, excreting waste, and thermoregulation. The integumentary organs include the skin and its appendages (hair, sebaceous glands, sweat glands, feathers, and nails) (*23*). The integumentary organs arise from organ germs through reciprocal epithelial-mesenchymal interactions in the skin field (*4*). During embryogenesis, the skin field forms through a regulated process of pattern formation, and its appendage organs are then induced through epithelial-mesenchymal interactions according to a typical Turing model of activator and inhibitor signals (*23*). Regeneration of the 3D IOS could contribute to regenerative therapies for patients with burns, scars, and alopecia, and could be used as a novel assay system for nonanimal safety testing of cosmetics and quasi-drugs (*5*, *24*). However, it is difficult to generate the complex 3D IOS using in vitro stem cell culture or in vivo transplantation models and to recapitulate the physiological functions of the skin using a bioengineered 3D IOS.

Here, we generated a bioengineered 3D IOS from iPS cells, which includes appendage organs such as hair follicles and sebaceous glands, using a novel in vivo transplantation model designated as the clustering-dependent embryoid body (CDB) transplantation method. We first developed the conditions for the induction of various epithelial germ layers in in vivo explants of iPS cells. Wnt signaling controlled the frequency of the 3D IOS, calculated by the number of hair follicles in the explants. After orthotopic transplantation of the bioengineered IOS into nude mice, the bioengineered hair follicles showed full functionality, including the ability to undergo repeated hair cycles through the rearrangement of various stem cell niches. Our current study thus demonstrates the development of a functional bioengineered 3D IOS and the realization of organ replacement therapy using iPS cells.

RESULTS

In vivo induction of epithelial tissue using a CDB transplantation method

To generate various epithelia from iPS cells, we first developed a CDB transplantation method as an in vivo transplantation model. To form the complete three-germ-layer epithelial tissue from iPS cells, we established iPS cells from murine gingiva (Fig. 1A) (*25*). In an in vitro culture of iPS cells (3000 cells per well of a 96-well plate), iPS cells formed embryoid bodies (EBs) in 3 days, and the EBs were allowed to grow for 1 week (Fig. 1B). The relative mRNA expression levels of undifferentiated iPS markers (*Nanog*) were significantly reduced over the culture period (Fig. 1C and table S1). By contrast, neural crest markers, such as *Nestin* and *Pax3*, were significantly increased on day 7 in culture (Fig. 1C). In an immunohistochemical analysis of EBs after 7 days in culture, we observed that the iPS cell–derived EBs had differentiated into both epithelial and mesenchymal cells (Fig. 1D). EBs expressed Sox2 and p63 as integumentary markers and expressed Sox17 as an endodermal epithelial marker. EBs also expressed proteins for the neural progenitor marker Pax6 and for neural crest markers such as Snail and Twist (Fig. 1D). These results indicated that both epithelial and mesenchymal cells were generated in iPS cell–derived EBs after 7 days in culture.

We next transplanted these EBs under various conditions into the subrenal capsule of severe combined immunodeficient (SCID) mice in vivo. Both single iPS cells and single EB transplants formed teratoma-like tissues, which contained three germ layers, including neural tissue, muscle, cartilage, and bronchial epithelia, as reported previously (Fig. 1E, top and middle) (*26*). By contrast, in multiple EBs transplanted using collagen gel, which contained more than 30 EBs cultured for 7 days under nonadhesive conditions (Fig. 1F), cystic epithelia were observed in the CDB transplants (Fig. 1E, bottom). The tissue weight of CDB transplants was heavy compared with single EB transplants, and organ formation was observed in 4 to 9 g of explants (Fig. 1G). The ratio of cystic tissue area in CDB transplants was significantly larger than that in explants of single iPS cells and single EB transplants (Fig. 1H and fig. S1).

We next characterized the types of epithelium generated in the in vivo explants using the CDB transplantation method, such as ectodermal epithelium, nerve tissue, integument, and endodermal epithelium, including the respiratory tract and gastrointestinal tube, by histochemical analyses with specific antibodies for CK5, CK10, Muc2, Cdx2, Pax6, villin, Tuj1, CC10, and E-cadherin (Fig. 1I and fig. S2). In the explants, we identified various types of epithelium arising from the three germ layers, including ectodermal epithelium (CK5-positive), integument (CK10-positive), and endodermal epithelium, including the respiratory tract (Muc2-positive, CC10-positive, and CK10-negative) and gastrointestinal tube (villin-positive and Cdx2-positive). Although the transplantation of single ES or iPS cells induced epithelium at low efficiency (*27*), the incidence ratio of epithelium was statistically constant in explants generated via the CDB transplantation method (Fig. 1J). These results indicate that our CDB transplantation method reproduced various epithelia.

Bioengineered 3D IOS in iPS cell–derived explants generated using the CDB transplantation method

In the iPS cell–derived explants generated via the CDB transplantation method, we observed that Wnt10b, which regulates the dermal papilla (DP) (*28*–*30*) and the subcutaneous adipose tissue (*31*) derived from neural crest origin, induced the bioengineered hair follicles and developed the stage of hair follicles compared with the not-stimulated condition (Fig. 2A). The morphology of EBs and the expression of Sox2, p63, Sox17, Pax6, Snail, and Twist were not different with or without Wnt10b signaling (Fig. 1D and fig. S3). The hair shaft in the explant is black (Fig. 2A), although the hair shaft of the SCID mouse is white, indicating that hair follicles contain melanocytes that originate from iPS cell–derived neural crest cells. Although the frequencies in the explants with or without Wnt10b signaling were not different (Fig. 2B), the number of bioengineered hair follicles in the CDB explants treated with Wnt10b was drastically higher than that of the explants without Wnt10b (Fig. 2C). In the explants treated with Wnt10b, the bioengineered hair shaft, which was measured from the tip of the hair shaft to the DP, was longer than that in the explants without Wnt10b (Fig. 2D). Moreover, the hair follicles in explants treated with Wnt10b were abundant, and mature hair follicle structures included the dermal sheath, DP, sebaceous glands, and subcutaneous adipose tissue (Fig. 2E). The expression of *Shh*, *Msx2*, *Wnt10b*, β-*catenin*, and *Lef1* in the epithelium, and of *Bmp4* and *Notch1* in the mesenchyme of the bioengineered hair follicles in the CDB explants cultured with Wnt10b, was similar to that observed in natural skin on embryonic day 18.5 (fig. S4) (*11*). Thus, in the iPS cell–derived explants generated via the CDB transplantation method, we observed the bioengineered 3D IOS, including the skin, hair follicles, dermis, sebaceous glands, and subcutaneous adipose tissue. We confirmed these structures using other iPS cell clones, including a gingiva-derived iPS cell clone (ectodermal origin), the stomach-derived iPS-Stm-FB/gfp-99-1 clone (endodermal origin), and the hepatocyte-derived iPS-Hep-FB/Ng/gfp-103C-1 clone (endodermal origin) (*32*). The gingiva- and stomach-derived iPS cell clones, but not the iPS-Hep-FB/Ng/gfp-103C-1 clone, generated the bioengineered 3D IOS, including hair follicles. These results indicate that the generation of a bioengineered 3D IOS is not dependent on the origin of iPS cell clones from different germ layers because heterogeneity exists among iPS cell clones.

In hair follicles, various stem cell types are maintained in particular regions, such as CD34-, CK15-, and Sox9-positive follicle epithelial cells in the follicle stem cell niche of the bulge region (*33*, *34*), Lrig1-positive epithelial stem cells in the upper bulge outer root sheath region, and multipotent mesenchymal precursors in DP cells (*34*, *35*). The follicle variable region mediates the hair cycle, which depends on the activation of Lgr5-positive follicle epithelial stem cells during the telogen-to-anagen transition. In addition, the follicle epithelial stem cells in the bulge region connect to the calponin-positive arrector pili muscles (Fig. 2F). We next investigated whether various stem/progenitor cells and their niches were reconstructed in the EGFP-labeled bioengineered hair follicles of the CDB transplants, which were produced using the EGFP-labeled iPS cell clone. All cells composed of bioengineered 3D IOS showed green fluorescence (Fig. 2G, left panels). Sox9 and CD34 double-positive epithelial stem cells were also observed in the bulge region of the normal iPS-derived bioengineered hair follicles (Fig. 2G). Lrig1-positive epithelial stem cells and Lgr5-positive epithelial cells were also observed in the proper anatomical regions, which were detected in the upper and lower portions of the CK15-positive bulge region, respectively (Fig. 2G). The calponin-positive arrector pili muscle was connected to the bulge region epithelial cells of both the natural hair follicle and the bioengineered hair follicle (Fig. 2H). These results indicate that various follicle stem cells and the arrector pili muscles were correctly arranged in the bioengineered hair follicles constructed using the bioengineered 3D IOS, which was derived from iPS cells.

Orthotopic transplantation of the iPS cell–derived bioengineered 3D IOS

We next investigated whether the iPS cell–derived IOS could be transplanted into the cutaneous environment of adult nude mice (Fig. 3A, upper panel). We isolated male cystic tissues with hair follicles in the explants, cut them into small specimens containing 10 to 20 follicular units, and transplanted them onto the backs of female nude mice using a follicular unit transplantation method (Fig. 3A, lower panels). At 14 days and thereafter, we observed the eruption and growth of black hair shafts (n = 216; Fig. 3B). After 3 months, we did not observe tumorigenesis in the transplantation areas (n = 171). To confirm that the transplanted 3D IOS was of iPS cell origin, we performed Y-chromosome fluorescence in situ hybridization (Y-FISH) with male mouse–specific DNA probes (Fig. 3C and fig. S5). Y-FISH–positive cells were observed in the transplantation area (including the skin epithelium, dermis, sebaceous glands, intracutaneous adipose tissue, and hair follicles) of the cervical skin of recipient female mice. These results indicated that the bioengineered IOS could engraft in the cervical skin and revealed that it is of iPS cell origin. The engrafted hair follicle must establish proper connections with the surrounding tissues, such as the arrector pili muscles and nerve fibers. The hair follicles in the bioengineered 3D IOS had connected to calponin-positive arrector pili muscles in the correct polarization to iPS cell–

[1]Department of Biological Science and Technology, Graduate School of Industrial Science and Technology, Tokyo University of Science, Noda, Chiba 278-8510, Japan. [2]Laboratory for Organ Regeneration, RIKEN Center for Developmental Biology, Kobe, Hyogo 650-0047, Japan. [3]Organ Technologies Inc., Minato-ku, Tokyo 105-0001, Japan. [4]Department of Regenerative Medicine, Plastic and Reconstructive Surgery, Kitasato University of Medicine, Sagamihara, Kanagawa 252-0374, Japan. [5]Research Institute for Science and Technology, Tokyo University of Science, Noda, Chiba 278-8510, Japan. [6]Division of Molecular and Regenerative Prosthodontics, Tohoku University Graduate School of Dentistry, Sendai, Miyagi 980-8575, Japan.
*These authors contributed equally to this work.
†Corresponding author. Email: t-tsuji@cdb.riken.jp

Originally published 1 April 2016 in *SCIENCE ADVANCES*

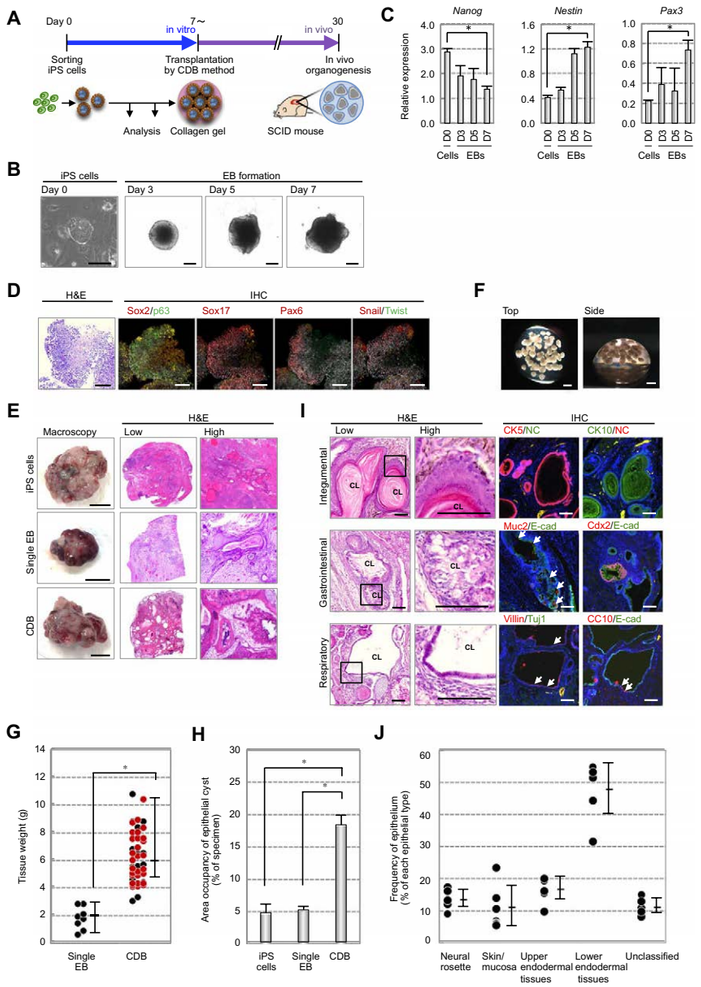

Fig. 1. Induction of epithelial tissues via the CDB transplantation method. (**A**) Schematic representation of EB cultures and the CDB transplantation method. (**B**) Phase-contrast images of iPS cells and the formation of EBs, which were cultured in nonadherent plastic wells for 3, 5, or 7 days. Scale bars, 100 μm. (**C**) mRNA expression levels of undifferentiated iPS cell markers (*Nanog*) and neural crest cell markers (*Nestin* and *Pax3*) during EB formation. *P < 0.001 by Student's t test. (**D**) Hematoxylin and eosin (H&E) staining and immunostaining of EBs, using antibodies of epithelial (Sox2/p63 and Sox17), neural progenitor (Pax6), and neural crest markers (Snail and Twist) after 7 days. The nuclei were stained using Hoechst 33258 (white). Scale bars, 50 μm. (**E**) Macroscopic photographs (left panels) and microscopy (H&E staining, center and right panels) of in vivo transplants under various transplantation conditions. The in vivo transplants of 3000 dissociated iPS cells (upper), single EBs (middle), and more than 30 EBs (lower) were placed in the subrenal capsule for 30 days and then analyzed. (**F**) Macroscopic photographs of multiple EB in a collagen gel before transplantation. Scale bars, 1 mm. (**G**) Weight of the in vivo transplants. The data are presented as the median ± maximum or minimum from individual experiments; n = 8 and n = 48 per experiment. Red circles indicate the cyst, including hair follicles, in the explants. *P < 0.001 by Student's t test. (**H**) The area occupancy of the cystic lumen in the whole specimens of in vivo transplants of the three types of conditions was compared. *P < 0.001 by Student's t test. (**I**) Histochemical and immunohistochemical analyses of the cystic epithelia in the in vivo explants of multiple iPS cell–derived EBs. Boxed areas in the left panels show H&E staining. To identify epithelial types, such as ectodermal epithelium, integument (top panels), and endodermal epithelium, including the gastrointestinal tube (middle panels) and respiratory tract (bottom panels), we analyzed CDB transplants by immunostaining with specific antibodies for CK5, CK10, Muc2, Cdx2, villin, CC10, Tuj1, and E-cadherin. The nuclei were stained using Hoechst 33258 (blue). To identify the nonspecific fluorescence signals in these immunohistochemical analyses, we performed the experiments under the conditions without specific antibodies against antigens [negative control (NC)]. Scale bars, 1 mm (low-magnification images) and 100 μm (high-magnification images). (**J**) The frequency of epithelial types in CDB transplants. Epithelial types in CDB transplants were classified based on the cell morphology and number count. The data are presented as the means ± SEM from individual experiments; n = 5.

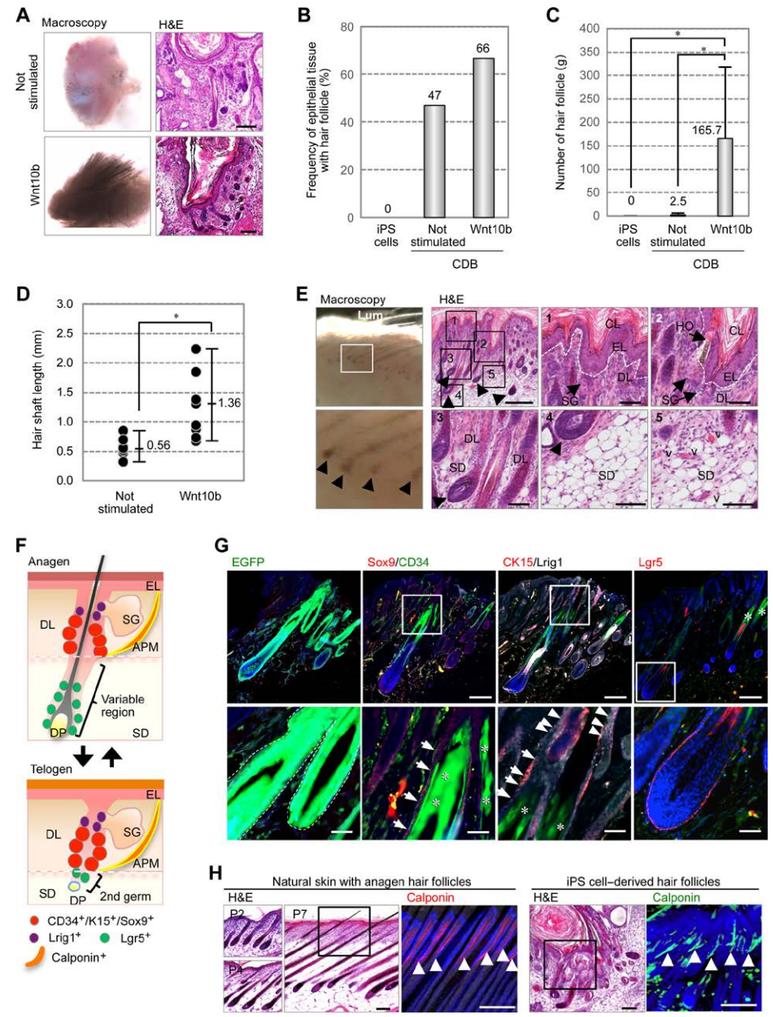

Fig. 2. Analysis of the bioengineered hair follicle induced from iPS cells via the CDB transplantation method. Macroscopic (left panels) and microscopic (H&E staining; right panels) examination of the hair follicles and shafts in the CDB transplants. EBs were stimulated without Wnt10b (upper panels) or with Wnt10b (lower panel) on day 7. Scale bars, 100 μm. (**B**) Frequency of the epithelial tissue, including hair follicle, in CDB transplants. The data are presented as the means ± SEM from individual experiments; n = 13 (single iPS injection), n = 49 (CDB transplants without Wnt10b), and n = 15 (CDB transplants with Wnt10b). (**C**) Number of hair follicles in the CDB transplants. The data are presented as the means ± SEM from individual experiments; n = 13 (single iPS injection), n = 74 (CDB transplants without Wnt10b), and n = 4 (CDB transplants with Wnt10b). *P < 0.001 by Student's t test. (**D**) Comparative analysis of the length of hair shafts from the hair tip to the DP in CDB explants treated with or without Wnt10b. *P < 0.05 by Student's t test. (**E**) Histological analysis of the hair follicles and their surrounding tissues in iPS cell–derived bioengineered 3D IOSs. The isolated cystic structures with hair follicles were observed macroscopically (left panels). In the H&E analyses, the boxed areas in the low-magnification macroscopic views are shown at a higher magnification in other panels. CL, cystic lumen; EL, epidermal layer; DL, dermal layer; SD, subdermal tissue; SG, sebaceous gland; HO, hair opening; v, vessel. Scale bars, 500 μm (H&E; upper left) and 100 μm (others). (**F**) Schematic representation of stem/progenitor cells in the hair follicle and surrounding tissues on the skin at the anagen and telogen phases. APM, arrector pili muscle. (**G**) Immunohistochemical analyses of stem/progenitor cells in the follicles of natural pelage and enhanced green fluorescent protein (EGFP)–labeled iPS cell–derived bioengineered hair follicles. These samples were immunostained with anti-Sox9 (red), anti-CD34 (green), anti-CK15 (red), anti-Lrig1 (white), and anti-Lgr5 (red) antibodies. Arrows, epithelial cells of bulge regions; arrowheads, Lrig1-positive cells; *, background fluorescence of hair shafts. Scale bars, 200 μm (upper panels) and 50 μm (lower panels). (**H**) Histological and immunohistochemical analyses of the iPS cell–derived hair follicles and their surrounding tissues. Natural pelage and iPS cell–derived hair follicles were stained with calponin. Arrowheads indicate calponin-positive arrector pili muscles. Scale bars, 200 μm.

derived follicles, which were identical to natural pelage follicles (Fig. 3D). Nerve fibers had also formed proper connections to the bulge region of the bioengineered hair follicles (Fig. 3D, lower panels). These results indicate that the iPS cell–derived hair follicles in the bioengineered IOS were correct in structure and established the proper connections to the surrounding tissues.

Analysis of iPS cell–derived hair species and distribution

We next investigated the hair species and their distribution in the bioengineered IOS in the cutaneous environment of recipient adult nude mice. The iPS cell–derived IOS produced all types of pelage hairs, including zigzag and awl/auchene and guard, in a similar population to the back skin of adult mice (Fig. 4, A and B) (*36*). We found that the distance between bioengineered hair follicles was not significantly different from that on the skin of normal mice (Fig. 4C). We further analyzed the distribution of hair shaft species in the transplanted iPS cell–derived IOS and compared the result with the natural skin of adult murine trunk region, including the body center and lumbar region of the side trunk lining on linea axillaris media (fig. S6). We also observed that the distribution of these hair species in the transplanted IOS was not significantly different from that in normal mice skin (fig. S6C). We further analyzed the hair cycles, which comprise alternating growth (hair growing) and regression (nongrowing) phases, of the iPS cell–derived hair follicles for 90 days (Fig. 4D). The iPS cell–derived follicles repeated the hair cycle at least three times during the transplantation period (Fig. 4D), and no significant differences in the hair cycle periods were found between natural and bioengineered follicles (both zigzag and awl/auchene and guard; Fig. 4E). These results suggest that the CDB transplantation method induced a skin field during early development by the subrenal capsule transplantation and generated the bioengineered IOS that behaved like natural mouse skin.

DISCUSSION

Our current findings reveal the generation of the bioengineered 3D IOS from iPS cells, including appendage organs such as hair follicles and sebaceous glands, with proper connections to surrounding tissues, including the epidermis, dermis, arrector pili muscles, fat, and nerve fibers, in an in vivo transplantation model—the CDB method. These findings significantly advance the technological development of bioengineered 3D IOS.

Studies of pluripotent stem cells have demonstrated the ability to generate whole embryos by tetraploid complementation in blastocysts and revealed that these cells can form teratomas, which include compartmentalized organized tissues derived from three germ layers, such as neural tissue (ectodermal), cartilage (mesenchymal), and gut/bronchial epithelia (endodermal), by an in vivo injection assay (*37*). Several cutaneous types of mature teratomas, such as cystic dermoids in the ovary and orbital regions, generate ectodermal organs, such as teeth and hair follicles (*17*). However, the molecular mechanisms underlying the development of these dermoids are still unknown. In an in vivo injection assay of ES and iPS cells, ectodermal organs could not be detected at a considerable frequency in pluripotent stem cell–derived teratomas. In 3D stem cell culture, bioengineered 3D tissues are limited to neuroectodermal and endodermal tissues (*2*). Thus, to generate a 3D IOS, we developed a novel CDB transplantation method to induce ectodermal tissues at a high frequency and successfully generated a 3D IOS in in vivo explants. In general, cultured EBs form an outer layer epithelial progenitor (*38*, *39*). Epithelium induction in our method may be due to the connection of the outer layer epithelium of each EB by self-assembly and self-formation in the explants. Furthermore, the frequency of hair follicles with sebaceous glands in the in vivo explants of our bioengineered 3D IOS could be controlled by Wnt signaling. Hence, our CDB transplantation method can be used to generate a bioengineered 3D IOS and contributes to our understanding of the molecular mechanisms of the onset of dermoid formation in vivo.

Wnt signaling pathways are essential for body patterning during embryogenesis and organ induction through epithelial-mesenchymal interactions (*40*). Wnt family molecules play important roles in forming an organ-forming field and the initial organ bud in both epithelial and mesenchymal tissues (*41*). Wnt10b signaling is known to play a key role in the progression of an initial organ bud to an organ germ, and also regulates the reciprocal epithelial-mesenchymal interactions of ectodermal organs, such as teeth, hair follicles, and exocrine organs (*28*). In hair follicle organogenesis, Wnt10b signaling regulates the differentiation from neural crest–derived mesenchyme into DP and the surrounding fat tissue (*30*, *42*, *43*). Here, the frequency of hair follicle formation, but not epithelial tissue formation, in in vivo explants was controlled by Wnt10b signaling in EBs. After treatment with Wnt10b on day 6 in culture, we detected the expression of neural crest markers, including *Nestin*, *Pax3*, *Snail*, and *Twist*. Therefore, our findings suggest that Wnt10b signaling plays important roles in the formation of hair follicles in the skin field, neural crest–derived melanocyte differentiation, and progression of organogenesis through reciprocal epithelial-mesenchymal interactions during morphogenesis.

For regenerative therapy in patients with burns, a cultured epithelial sheet is useful for the replacement of skin physiological functions, such as the protection of deeper tissues, waterproofing, and thermoregulation (*5*). However, it is well recognized that current therapies using cultured epithelial tissues suffer from critical issues, including aesthetics and the inability to excrete sweat and lipids from exocrine organs (*44*). In addition, artificial skin consisting of cultured epithelial epidermis and dermis without appendage organs and pores is often used for testing during the development of cosmetics and quasi-drugs, although this method has critical limitations related to the permeability of cosmetics and drugs and the reliability of physiological responses (*45*). By contrast, it is expected that bioengineered 3D IOS can overcome these issues (*46*). Here, we provide evidence for the generation of a 3D IOS from iPS cells using an in vivo transplantation model. The explants were fully functional and included hair follicles and sebaceous glands with proper connections to the surrounding tissues, such as the epithelium, dermis, fat, arrector pili muscles, and nerve fibers. Although the origin of nerve fibers is still unclear, nerve fibers would be innervated from host tissues. Our previous studies of ectodermal organ transplantations demonstrated that the innervation into the explants had been indicated from host tissues (*10*–*13*).

In conclusion, we generated a fully functional 3D IOS by the self-assembly of epithelial and mesenchymal stem cells from iPS cells using the CDB transplantation method. Our study contributes to the development of bioengineering technologies that will enable future regenerative therapies for patients with burns, scars, and alopecia. Further optimization of our technique using in vitro stem cell culture and humanization will contribute to the development of bioengineered IOS therapy as a prominent class of organ system replacement regenerative therapy and as a novel nonanimal assay system for cosmetics and quasi-drugs in the future.

METHODS

Cell culture of mouse iPS cells

The mouse iPS cell line "gingiva-derived iPS" was established by Egusa *et al.* (*25*) at Tohoku University. The iPS-Stm-FB/gfp-99-1 and iPS-Hep-FB/Ng/gfp-103C-1 lines were purchased from the RIKEN BioResource Center. All iPS cell lines were maintained in the presence of a mitomycin C–treated SNLP feeder layer on gelatin-coated dishes. The culture medium for these mouse iPS cells consisted of Dulbecco's modified Eagle's medium (DMEM) (Nacalai Tesque) supplemented with 15% fetal bovine serum (Biosera), 2 mM L-glutamine (Invitrogen), 1 × 10^{-4} M nonessential amino acids (Invitrogen), 1 × 10^{-4} M 2-mercaptoethanol (Invitrogen), penicillin (50 U/ml), and streptomycin (50 μg/ml; Invitrogen) (*25*).

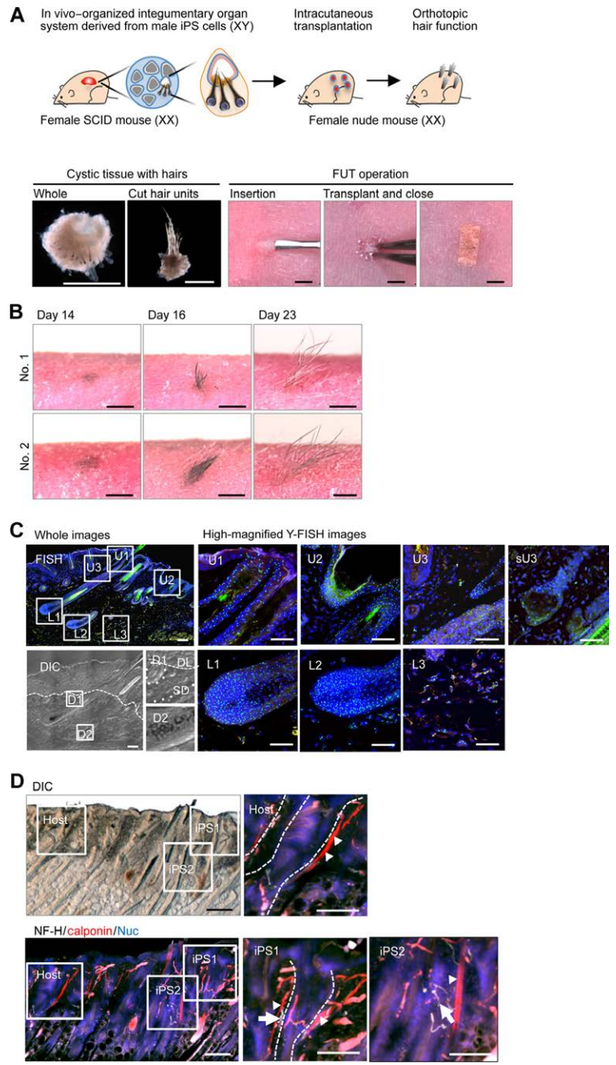

Fig. 3. Transplantation of the bioengineered 3D IOS. (**A**) Schematic representation of the methods used for the generation and transplantation of iPS cell–derived hair follicles. Cystic tissue with hair follicles was isolated and divided into small pieces containing 10 to 20 hair follicles (lower left panels). The small pieces were transplanted into the back skin of nude mice using a follicular unit transplantation (FUT) method developed in humans (lower right panels). Scale bars, 500 μm (lower left panels) and 1 mm (lower right panels). (**B**) Macromorphological observations of two independent engraftments into the dorsoventral skin of nude mice showing the eruption and growth of iPS cell–derived hair follicles. Scale bars, 1 mm. (**C**) Y-FISH analysis of the CDB transplants using male mouse–specific DNA probes. H&E and differential interference contrast (DIC) images are shown in the left panels. FISH images are shown in the upper left panel. Green and blue signals indicate Y-chromosome–positive cells and nuclei, respectively. Boxed areas in the FISH image are shown at a higher magnification in the right panels. Boxed areas U1 and U2 indicate the skin epithelium and upper region of the hair follicle. U3 indicates the bulge region. Boxed area sU3 indicates the Y-FISH–positive sebaceous gland isolated from fig. S5. Boxed areas L1 and L2 indicate the lower hair bulb region. Boxed area L3 indicates the intracutaneous adipose tissue. Broken lines in the differential interference contrast image indicate the outermost limit of the dermis. Scale bars, 200 μm (whole images) and 100 μm (high-magnification images). (**D**) Analysis of the integration with surrounding tissues, such as the arrector pili muscles and nerves, in the cervical skin of nude mice. The differential interference contrast images show black hair shafts derived from the bioengineered 3D IOS (origin: C57BL/6 mice) among the white hairs of nude mice. The arrector pili muscles and nerve fibers were analyzed by immunohistochemical staining using specific antibodies against calponin (red) for smooth muscle and neurofilament H (NF-H; white). The nuclei (Nuc) were stained using Hoechst 33258 (blue). The boxed areas in the left panels are shown at a higher magnification in the right panels. The arrows and arrowheads indicate nerve fibers and muscles connected with hair follicles, respectively. Broken lines indicate the outermost limit of each hair follicle. Scale bars, 200 μm (low-magnification photographs) and 100 μm (high-magnification photographs).

Induction of mouse iPS cell differentiation

Mouse iPS cells were harvested by dissociation using 0.25% trypsin-EDTA (Invitrogen) with feeder cells. Then, dissociated cells were separated into iPS cells and feeder cells using Feeder Removal MicroBeads (MACS; Miltenyi Biotec). For EB culture, the iPS cells were re-aggregated using Nunclon Sphera round-bottom 96-well plates (Thermo Fisher Scientific Inc.) in a culture medium (3000 cells/100 μl per well). Fresh medium was added to the culture on day 3, and Wnt10b (500 ng/ml; R&D Systems) was added on day 6.

Gene expression analysis by real-time PCR

Total RNA was isolated from mouse iPS cells or EBs using TRIzol reagent (Life Technologies) according to the manufacturer's protocol. Reverse transcription was performed with the PrimeScript II 1st strand cDNA Synthesis Kit (TaKaRa Bio). The mRNA expression levels were determined using SYBR Premix Ex Taq II (TaKaRa Bio), and the products were analyzed with an Applied Biosystems QuantStudio 12K Flex (Life Technologies). The data were normalized to β-actin expression. The primer pairs used for real-time polymerase chain reaction (PCR) are listed in table S1. For quantitative analysis, 32 to 48 EBs were analyzed in triplicate in each experiment, which was repeated at least three times.

Animals

C.B-17/Icr-*scid*/*scid*Jcl mice were purchased from CLEA Japan Inc., and C57BL/6NCrSlc and Balb/c nu/nu mice were purchased from Japan SLC Inc. Animal care and handling conformed to the National Institutes of Health guidelines, the requirements of the Tokyo University of Science Animal Care and Use Committee (permit no. N13008), and the

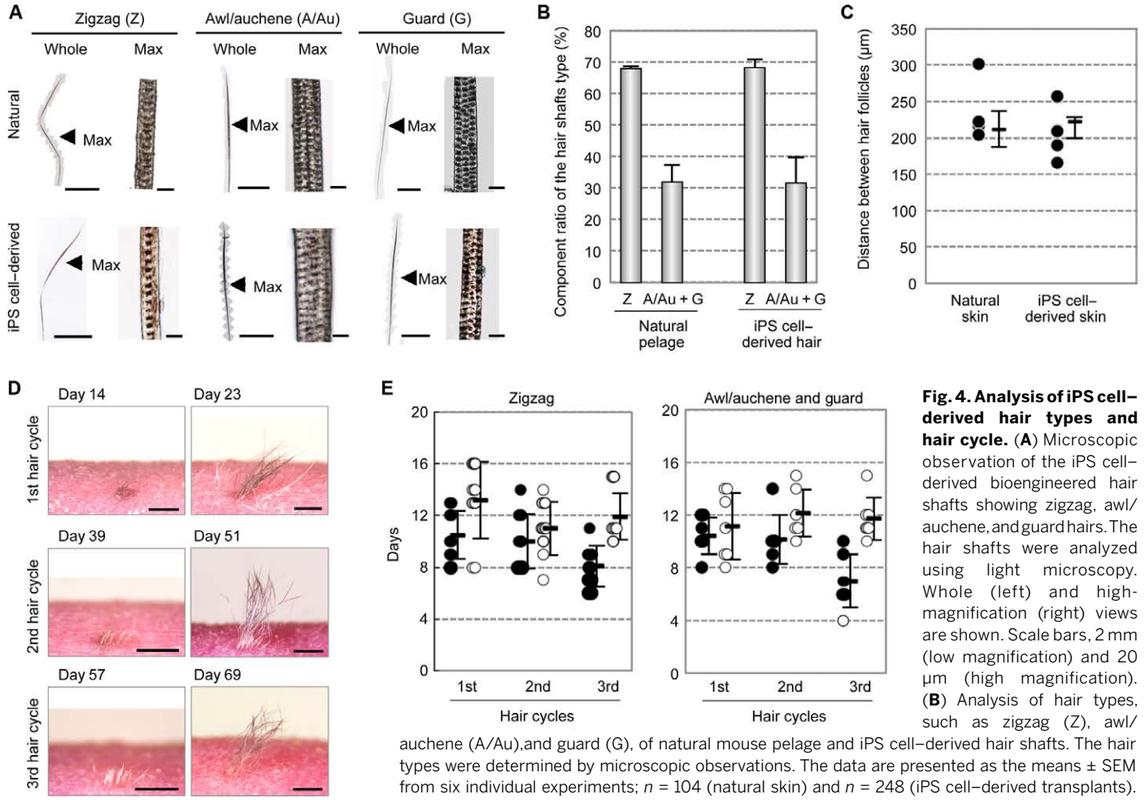

Fig. 4. Analysis of iPS cell–derived hair types and hair cycle. (**A**) Microscopic observation of the iPS cell–derived bioengineered hair shafts showing zigzag, awl/auchene, and guard hairs. The hair shafts were analyzed using light microscopy. Whole (left) and high-magnification (right) views are shown. Scale bars, 2 mm (low magnification) and 20 μm (high magnification). (**B**) Analysis of hair types, such as zigzag (Z), awl/auchene (A/Au),and guard (G), of natural mouse pelage and iPS cell–derived hair shafts. The hair types were determined by microscopic observations. The data are presented as the means ± SEM from six individual experiments; n = 104 (natural skin) and n = 248 (iPS cell–derived transplants). (**C**) Distance between hair shafts in natural pelage and iPS cell–derived bioengineered hair shafts. The distances were calculated by microscopic observations of H&E-stained sections. The data are presented as the means ± SEM from individual experiments; n = 6 (natural skin) and n = 6 (iPS cell–derived transplants). (**D**) Macromorphological observations at the anagen phase of the hair cycles in iPS cell–derived bioengineered hair. Scale bars, 1 mm. (**E**) Assessment of the hair growth (closed circles) and regression (open circles) phases of the bioengineered hair, including zigzag and awl/auchene and guard hair types. The data are presented as the means ± SEM; n = 5 (zigzag) and n = 10 (awl/auchene and guard).

Guidelines for Use of Laboratory Animals of RIKEN and Use Committee (AH26-02-3).

iPS cell–derived EB transplantation and extraction

EBs cultured for 7 days were selected, and 48 (not stimulated) and 32 (Wnt10b stimulated) EBs were sterilely placed in a 20-μl collagen gel drop (Nitta Gelatin Inc.). The collagen gel drop was transplanted into the subrenal capsules of 6-week-old C.B-17/lcr-*scid/scid*Jcl mice. Thirty days after the transplantation of iPS-EBs, the in vivo transplants were extracted, divided into five equal parts, and placed into DMEM (WAKO) containing 10% fetal calf serum (GIBCO), penicillin (100 U/ml; Sigma), streptomycin (100 mg/ml; Sigma), and 20 mM Hepes (Invitrogen) on ice. They were treated with collagenase (100 U/ml; Worthington) for 10 min at 37°C and washed with medium to separate the organs for in vivo transplants. The iPS cell–derived 3D IOS was dissected using a surgical knife under a microscope.

Engraftment of the iPS cell–derived 3D IOS

For hair follicle regeneration, the iPS cell–derived hair follicles, which were divided into small pieces containing 10 to 20 hair follicles, were intracutaneously transplanted into the back skin of 6-week-old Balb/c nu/nu mice, as previously described (*47*). Shallow stab wounds were made on the back skin of nude mice using a 20-gauge Ophthalmic V-Lance (Alcon Japan). The iPS cell–derived 3D IOSs were held so that the hair protruded from the skin surface. The transplantation sites were then covered with surgical bandage tape (Nichiban). To examine the engraftment of the transplants and to study the hair cycles of the bioengineered hairs, we observed all transplanted sites using the SteREO Lumar. V12 and AxioCam fluorescent stereoscopic microscope system (Carl Zeiss). Observations were made every 2 to 3 days.

Immunohistochemistry

Paraffin sections (10 μm) were stained with H&E and observed using an Axio Imager A1 (Carl Zeiss) or an Axio Scan.Z1 (Carl Zeiss). For fluorescent immunohistochemistry, frozen sections (10 and 100 μm) and paraffin sections (10 μm) were prepared and immunostained as previously described (*11*, *12*). Before immunostaining, frozen sections of EGFP-labeled samples were treated with or without Superfix (KURABO) for 30 min at room temperature. The primary antibodies used were as follows: CK5 (1:100, rabbit; Covance), CK10 (DE-K10) (1:100, rabbit; Abcam), Muc2 (H-300) (1:100, rabbit; Santa Cruz Biotechnology), Cdx2 (EPR2764Y) (1:250, rabbit; Abcam), Pax6 (1:200, rabbit; Covance), calponin (EP798Y) (1:250, rabbit; Abcam), CK15 (1:2000, chicken; Abcam), Sox9 (1:100, mouse; Abcam), CD34 (MEC 14.7) (1:100, rat; Abcam), Lrig1 (1:400, goat; R&D Systems), Lgr5 (1:100, rabbit; Abcam), neurofilament H (TA51) (1:500, rat; Chemicon), villin (C-19) (1:200, goat; Santa Cruz Biotechnology), CC10 (T-18) (1:100, goat; Santa Cruz Biotechnology), Tuj1 (TU-20) (1:200, mouse; Chemicon), and E-cadherin (36/E-Cadherin) (1:200, mouse; BD Biosciences) in blocking solution. The primary antibodies were detected using highly cross-absorbed Alexa Fluor 488 donkey anti-mouse immunoglobulin G (IgG; H + L) (1:500; Life Technologies), Alexa Fluor 488 goat anti-rat IgG (H + L) (1:500; Life Technologies), Alexa Fluor 488 donkey anti-rabbit IgG (H + L) (1:500; Life Technologies), Alexa Fluor 594 donkey anti-mouse IgG (H + L) (1:500; Life Technologies), Alexa Fluor 594 donkey anti-goat IgG (H + L) (1:500; Invitrogen), Alexa Fluor 594 donkey anti-rabbit IgG (1:500; Invitrogen), Alexa Fluor 594 goat anti-rabbit IgG (H + L) (1:500; Life Technologies), or Alexa Fluor 633 goat anti-rat IgG (H + L) (1:500; Invitrogen) with Hoechst 33258 dye (1:500; Dojindo) for 1 hour at room temperature. All fluorescence microscopy images were obtained with an LSM 780 confocal microscope (Carl Zeiss) or an Axio Scan.Z1 (Carl Zeiss).

Mouse Y-FISH

To detect male-origin iPS cell–derived 3D IOSs engrafted into female mouse skin, we performed mouse Y-FISH on 10-μm paraffin sections using fluorescein isothiocyanate–conjugated murine Y-chromosome probes (Chromosome Science Labo Inc.). All fluorescence microscopy images were captured on an LSM 780 confocal microscope (Carl Zeiss).

In situ hybridization

In situ hybridizations were performed using 10-μm frozen sections as described previously (*11*). Briefly, digoxigenin-labeled probes for specific transcripts were prepared by PCR with published primers. The mRNA expression patterns were visualized according to the immunoreactivity with anti-digoxigenin alkaline phosphatase–conjugated Fab fragments (Roche) according to the manufacturer's instructions.

Analyses of the distance between hair follicles and the distribution of hair shaft species

Skin samples from C57BL/6NCrSlc mice were dissected from three different regions, including the thorax, body center, and lumbar region of the side trunk lining on murine linea axillaris media. The iPS cell–derived IOSs, which were divided into small pieces containing 10 to 20 hair follicles from in vivo explants, were intracutaneously transplanted into the back skin of 6-week-old Balb/c nu/nu mice, as described above. The iPS cell–derived skins after transplantation were dissected at the first or second anagen phase. The natural skins and iPS cell–derived skin were fixed and placed horizontally on a plastic dish before macroscopic photographs were taken. To examine the hair types and distribution of the species of hair shafts, we observed all samples using the SteREO Lumar.V12 and AxioCam microscope system (Carl Zeiss). The distance between hair pores was measured with AxioVision Vs40 Image processing software (Carl Zeiss). The position of natural and iPS cell–derived hair pores, hair growth direction, and species of hair shafts (classified as zigzag and awl/auchene and guard) in 1-mm^2 portions were analyzed by the methods described previously (*36*).

REFERENCES AND NOTES

1. M. Takeichi, *Dev. Cell* **21**, 24–26 (2011).
2. Y. Sasai, *Cell Stem Cell* **12**, 520–530 (2013).
3. Y. Sasai, *Nature* **493**, 318–326 (2013).
4. J. Pispa, I. Thesleff, *Dev. Biol.* **262**, 195–205 (2003).
5. B. K. Sun, Z. Siprashvili, P. A. Khavari, *Science* **346**, 941–945 (2014).
6. T.-T. Sun, H. Green, *Cell* 9, **511**–521 (1976).
7. A. Atala, *Lancet* **385**, 487–488 (2015).
8. P. T. Sharpe, C. S. Young, *Sci. Am.* **293**, 34–41 (2005).
9. K. Nakao *et al.*, *Nat. Methods* **4**, 227–230 (2007).
10. E. Ikeda *et al.*, *Proc. Natl. Acad. Sci. U.S.A.* **106**, 13475–13480 (2009).
11. K.-e. Toyoshima *et al.*, *Nat. Commun.* **3**, 784 (2012).
12. M. Ogawa *et al.*, *Nat. Commun.* **4**, 2498 (2013).
13. M. Hirayama *et al.*, *Nat. Commun.* **4**, 2497 (2013).
14. S. M. Wu, K. Hochedlinger, *Nat. Cell Biol.* **13**, 497–505 (2011).
15. D. E. Cohen, D. Melton, *Nat. Rev. Genet.* **12**, 243–252 (2011).
16. E. Walck-Shannon, J. Hardin, *Nat. Rev. Mol. Cell Biol.* **15**, 34–48 (2014).
17. F. A. Tavassoli, P. Devilee, Eds., *Pathology and Genetics of Tumours of the Breast and Female Genital Organs. World Health Organization Classification of Tumours* (IARC Press, Lyon, France, 2003), 432 pp.
18. M. Eiraku *et al.*, *Nature* **472**, 51–56 (2011).
19. H. Suga *et al.*, *Nature* **480**, 57–62 (2011).
20. T. Nakano *et al.*, *Cell Stem Cell* **10**, 771–785 (2012).
21. K. R. Koehler, A. M. Mikosz, A. I. Molosh, D. Patel, E. Hashino, *Nature* **500**, 217–221 (2013).
22. C. L. Watson *et al.*, *Nat. Med.* **20**, 1310–1314 (2014).
23. T.-X. Jiang *et al.*, *Int. J. Dev. Biol.* **48**, 117–135 (2004).
24. Y. Fukano *et al.*, *Wound Repair Regen.* **14**, 484–491 (2006).
25. H. Egusa *et al.*, *PLOS One* **5**, e12743 (2010).
26. K. Okita, M. Nakagawa, H. Hyenjong, T. Ichisaka, S. Yamanaka, *Science* **322**, 949–953 (2008).
27. J. T. Fujii, G. R. Martin, *J. Embryol. Exp. Morphol.* **74**, 79–96 (1983).
28. S. Reddy *et al.*, *Mech. Dev.* **107**, 69–82 (2001).
29. J. Fu, W. Hsu, *J. Invest. Dermatol.* **133**, 890–898 (2013).
30. Y. Ouji, F. Nakamura-Uchiyama, M. Yoshikawa, *Biochem. Biophys. Res. Commun.* **438**, 493–499 (2013).
31. S. E. Ross *et al.*, *Science* **289**, 950–953 (2000).
32. T. Aoi *et al.*, *Science* **321**, 699–702 (2008).
33. R. J. Morris *et al.*, *Nat. Biotechnol.* **22**, 411–417 (2004).
34. F. M. Watt, *Science* **346**, 937–940 (2014).
35. C. A. B. Jahoda, C. J. Whitehouse, A. J. Reynolds, N. Hole, *Exp. Dermatol.* **12**, 849–859 (2003).
36. R. R. Driskell, A. Giangreco, K. B. Jensen, K. W. Mulder, F. M. Watt, *Development* **136**, 2815–2823 (2009).
37. K. Takahashi, S. Yamanaka, *Cell* **126**, 663–676 (2006).
38. C. M. Metallo, L. Ji, J. J. de Pablo, S. P. Palecek, *Stem Cells* **26**, 372–380 (2008).
39. T. Kadoshima *et al.*, *Proc. Natl. Acad. Sci. U.S.A.* **110**, 20284–20289 (2013).
40. A. Stathopoulos, M. Levine, *Dev. Cell* **9**, 449–462 (2005).
41. L. Jiménez-Rojo, Z. Granchi, D. Graf, T. A. Mitsiadis, *Front. Physiol.* **3**, 107 (2012).
42. M.-X. Lei, C.-M. Chuong, R. B. Widelitz, *J. Invest. Dermatol.* **133**, 7–9 (2013).
43. X. Lim, R. Nusse, *Cold Spring Harb. Perspect. Biol.* **5**, a008029 (2013).
44. C. Niemann, F. M. Watt, *Trends Cell Biol.* **12**, 185–192 (2002).
45. E. E. Kandyba, M. B. Hodgins, P. E. Martin, *J. Invest. Dermatol.* **128**, 1039–1049 (2008).
46. E. Bellas, M. Seiberg, J. Garlick, D. L. Kaplan, *Macromol. Biosci.* **12**, 1627–1636 (2012).
47. K. Asakawa *et al.*, *Sci. Rep.* **2**, 424 (2012).

ACKNOWLEDGMENTS

We are grateful to T. Irie for the invaluable comments. **Funding:** This work was partially supported by a Grant-in-Aid for KIBAN (A) from the Ministry of Education, Culture, Sports, Science, and Technology (grant 25242041) and by a collaboration grant (to T.T.) from Organ Technologies Inc. This work was partially funded by Organ Technologies Inc. **Author contributions:** T.T. designed the research plan; R.T., J.I., A. Sugawara, K.-e.T., K.I., M. Ogawa, K.S., K.A., A.K., M. Oshima, and R.M. performed the experiments; A. Sato, T.Y., A.T., H.E., and T.T. discussed the results; and T.T., K.-e.T., and M. Ogawa wrote the paper. **Competing interests:** This work was performed under an invention agreement between the Tokyo University of Science, RIKEN, and Organ Technologies Inc. T.T. is a director at Organ Technologies Inc. **Data and materials availability:** All data needed to evaluate the conclusions in the paper are present in the paper and/or the Supplementary Materials. Additional data related to this paper may be requested from the authors.

SUPPLEMENTARY MATERIALS

http://advances.sciencemag.org/cgi/content/full/2/4/e1500887/DC1
Supplementary Text
Fig. S1. Analysis of the area of the cystic lumen.
Fig. S2. Histochemical and immunohistochemical analyses of the cystic epithelia in the in vivo explants of multiple iPS cell–derived EBs.
Fig. S3. Culture of iPS cells for EB formation.
Fig. S4. Gene expression in iPS cell–derived bioengineered hair follicle germs in a 3D IOS generated via the CDB transplantation method.
Fig. S5. Y-FISH analysis of the distribution of iPS cell–derived cells among the 3D IOSs grafted to the natural murine skin.
Fig. S6. Distribution of hair species of iPS cell–derived hairs.
Table S1. Primer sequences used in real-time PCR.

Submitted 6 July 2015; Accepted 29 February 2016
Published 1 April 2016
10.1126/sciadv.1500887

Citation: R. Takagi, J. Ishimaru, A. Sugawara, K.-e. Toyoshima, K. Ishida, M. Ogawa, K. Sakakibara, K. Asakawa, A. Kashiwakura, M. Oshima, R. Minamide, A. Sato, T. Yoshitake, A. Takeda, H. Egusa, T. Tsuji, Bioengineering a 3D integumentary organ system from iPS cells using an in vivo transplantation model. *Sci. Adv.* **2**, e1500887 (2016).

The Fast module for ZEISS LSM 880 with Airyscan:

Confocal superresolution imaging with four times the speed and improved signal-to-noise ratio

Author: Joseph Huff, PhD
Carl Zeiss Microscopy, LLC, Thornwood, NY, USA

Dr. Annette Bergter
Carl Zeiss Microscopy GmbH, Germany

Date: April 2016

First introduced in August 2014, the Airyscan detector from ZEISS represents a new detector concept for laser-scanning microscopy (LSM) that enables a simultaneous resolution and signal-to-noise (SNR) increase over traditional LSM imaging. The Airyscan detector design substitutes the conventional LSM detector and pinhole scheme for an array of 32 sensitive GaAsP detector elements, arranged in a compound eye fashion that resides in the pinhole-plane while still generating an optical section. The new detection geometry allows for the collection of the spatial distribution of light originating from every point of a microscopic fluorescent object at the pinhole allowing access to higher frequency information and while additionally collecting more light for ultra-efficient imaging. Based on the Airyscan detection concept, the next innovation from ZEISS has been developed with the introduction of the Fast mode for Airyscan. The Fast mode concept utilizes the Airyscan detector technology in combination with an illumination shaping approach to enhance acquisition speeds by four times while simultaneously increasing SNR and resolution overcoming the traditional compromises of LSM imaging.

Introduction

The Confocal Laser Scanning Microscope (LSM) has become one of the most popular instruments in basic biomedical research for fluorescence imaging. The main reason LSM has become so popular is that the technique affords researchers images with high contrast and a versatile optical sectioning capability to investigate three dimensional biological structures [1]. The optical sectioning ability of an LSM is a product of scanning a diffraction limited spot, produced by a focused laser spot, across a sample to create an image one point at a time. Traditionally, the generated fluorescence for each point is collected and focused back through an aperture (pinhole) onto a unitary detector (typically a PMT). The traditional detection scheme allows the pinhole to reject the out of focus light and the PMT to turn the remaining light from the focal plane into a digital signal to form an optical sectioned image [2]. As confocal systems developed over the past 25 years, all major developments of commercially available systems focused on novel methods to increase image contrast, instrument versatility and acquisition speed. These innovations have provided the LSM with the flexibility to address research applications in many areas, providing data of cell differentiation, cell tracking, live cell kinetics, protein expression, protein localization, neural network connectivity, tissue structure, gene expression and protein / gene function (list is not meant to be inclusive). However, until the introduction of the Airyscan detection concept, the LSM system flexibility has always forced a researcher into making a compromise on a performance metric of a system in order to increase another (i.e. speed for resolution, resolution for SNR etc) to meet application requirements. The introduction of both the Airyscan detection concept in 2014 and now the Airyscan Fast mode represents a fundamental change where traditional imaging compromises no longer exist and all metrics can be improved simultaneously.

Improving Resolution and SNR on a Confocal

The Airyscan detector design simultaneously improves SNR and resolution with a hexagonally packed 32 channel GaAsP PMT array that is positioned in the pinhole plane (Fig. 1) and removing the traditional pinhole-PMT scheme. This concept combined two preferable but opposed / conflictive settings of the pinhole in the traditional LSM; an open pinhole would allow a lot of light to pass and thus increasing signal to noise, while a small pinhole opening will improve the resolution of the system. Further, each of the 32 detector elements behaves as a small independent pinhole where not only the optical resolution is improved but also spatial distribution of the light is recoded to additionally improve the spatial frequency contrast of the LSM system beyond what a traditional system provides. To use Airyscan for super resolution imaging, the adjustable zoom optics can be arranged to project 1.25 Airy units onto the detector where each detector element represents 0.2 Airy units yielding a 1.4 x optical resolution improvement and collect up to 50 % more light than an traditional LSM system with a 1 AU pinhole. Once combined with a linear deconvolution, a 1.7 x resolution improvement in all three dimensions is achieved and the additional collection efficiency of the detector provides a 4x – 8x SNR improvement affording researchers the ability to better quantify and study biological processes like microtubule buckling as a measure of measure of mechanical stress on a cell. (Fig. 2, [3]).

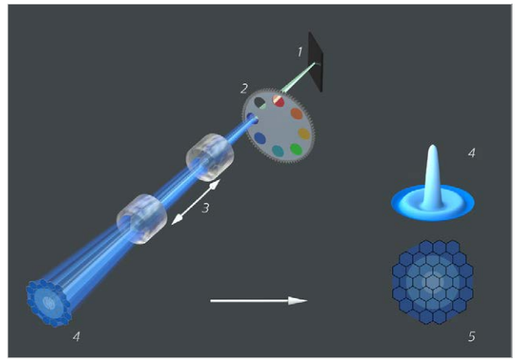

Figure 1 *Schematic of Airyscan detector for LSM 880*
1. Mirror 2. Emission filters 3. Zoom optics 4. Airy disk 5. Airyscan detector

Improving Speed on a Point Scanning Confocal

Traditionally in order to improve acquisition speeds on a point scanning confocal system, the speed at which the laser spot rasters the field of view is increased resulting in a decrease the amount of time the laser spot spends on one pixel. For the maximum speed increase, resonance scanning approaches are utilized in LSM systems allowing frame rates of around 30 Hz for a full field of view. However, to achieve the higher acquisition rates a researcher will have to sacrifice the resulting SNR of an image. The reason for the image SNR decrease is that as the acquisition speed is increased, the laser spot will spend less time per pixel and thus fewer photons will be available resulting in a deterioration of image SNR (Fig. 3, upper panel). At some point the SNR can get so low, that it becomes impossible to discriminate individual features of the sample and structural information is lost in the process to reach the necessary temporal resolution, rendering the method non-usable for the aspired scientific goal.

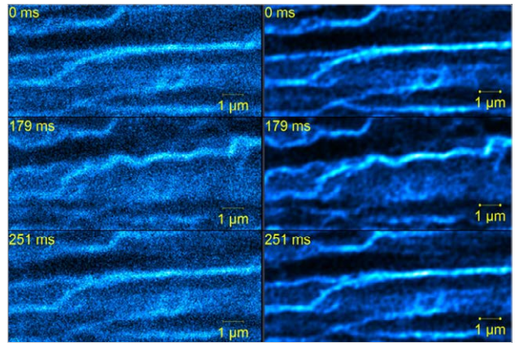

Figure 2 *Application example of standard confocal compared to Airyscan detection using cardiomyocyte Cells with SiR-tubulin to measure microtubule buckling. (Left Panel) Traditional confocal still images from a timeseries acquired at 30 fps with low SNR. (Right Panel) Airyscan still images from a time series acquired at 30 frames/sec with high SNR and resolution. Each series of stills represents the resting tubules, contracted tubules, and resting tubules respectively. Images courtesy of Ben Prosser, University of Pennsylvania [3]*

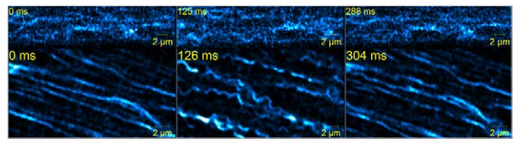

Figure 3 *Application example of a resonance scanning time series compared to a time series from the Airyscan Fast acquisition mode using cardiomyocyte Cells with tubulin-EMTB to measure microtubule buckling at high frame rates. (Top panel) Still images from a resonance scanning time series acquired at 80 frames/sec. (Bottom panel) Still images from an Airyscan Fast mode time series acquired at 96 frames/sec. Each series of stills represents the resting tubules, contracted tubules, and resting tubules respectively. Images courtesy of Ben Prosser, University of Pennsylvania [3]*

To overcome the trade-off between acquisition speed and image SNR, the Airyscan detector concept has been combined with an illumination shaping approach for a new fast acquisition mode. The innovation of the new acquisition mode utilizes the concept of excitation and detection parallelization to increase frame rates to avoid sacrificing SNR. Subsequently, in the new Fast mode approach the excitation beam is shaped to illuminate four lines in parallel and the Airyscan area detector collects data from all four lines simultaneously (Fig. 4). By employing a parallelization approach, acquisition speeds are increased by a factor of 4 while keeping high pixel dwell times resulting in a high image SNR. Hence, while increasing imaging speed notably, high signal to noise ratios can be preserved resulting in meaningful data. Moreover, since the Fast mode approach is based on the Airyscan detector, the additional simultaneous increase in SNR and resolution remain. Therefore Airyscan in Fast mode offers a researcher the unprecedented combination of a 1.5 x resolution increase and 4 x SNR increase at four times the acquisition speed (Fig. 3, lower panel).

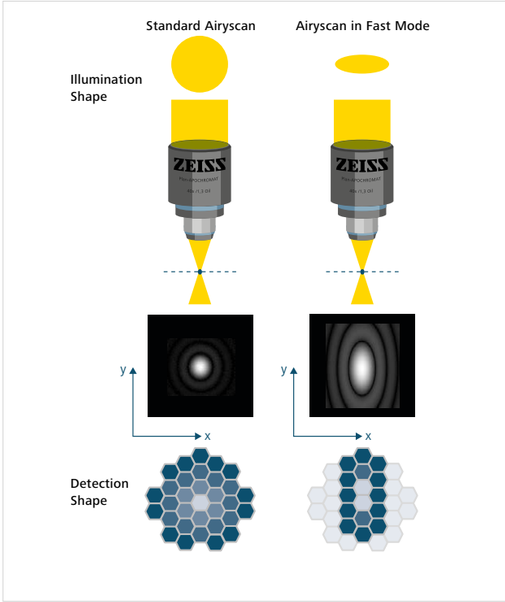

Figure 4 *(Left Panel) The illumination and detection scheme of the standard Airyscan mode where a diffraction limited spot is projected into the sample and the associated Airy disc from the collected fluorescence is projected onto all 32 elements of the Airyscan detector. (Right Panel) The illumination spot is elongated in the y dimension to cover four lines simultaneously and 16 channels of the Airyscan detector are utilized collect the emission from all four lines simultaneously*

Summary

In summary, the Airyscan detection module dispenses with the classical physical pinhole and unitary detector assembly and utilizes a new pinhole-plane image detection assembly based on a novel 32 channel GaAsP-PMT area detector. In 2014 Airyscan was implemented to provide a flexible and robust method to substantially increase resolution and signal-to-noise compared to traditional confocal LSM. Using the Airyscan detector design for new innovation, Fast mode for Airyscan provides a substantial increase in speed while simultaneously providing increases in resolution and signal-to-noise compared to traditional confocal LSM.

References:

[1] Conchello, J.-A. and J. W. Lichtman, Optical sectioning microscopy. Nature methods, 2005. 2(12): p. 920 – 931.

[2] Neu, T.R. and J.R. Lawrence, Innovative techniques, sensors, and approaches for imaging biofilms at different scales. Trends in Microbiology, 2015.

[3] Robison et Al, “Detyrosinated microtubules buckle and bear load in contracting cardiomyocytes”, Science April 2016

[5] Sheppard, C.J., Super-resolution in confocal imaging. Optik, 1988. 80(2): p. 53 – 54.

[6] Sheppard, C.J., S.B. Mehta, and R. Heintzmann, Superresolution by image scanning microscopy using pixel reassignment. Opt Lett, 2013. 38(15): p. 2889 – 2892.

[7] Huff, J., The Airyscan detector from ZEISS: confocal imaging with improved signal-to-noise ratio and super-resolution. Nature methods, 2015. 12.

[8] Weisshart, K., The basic principle of Airyscanning. 2014. ZEISS Technology Note

[9] Huff, J.; Bathe, W.; Netz, R.; Anhut, T.; Weisshart, K., The Airyscan detector from ZEISS. Confocal imaging with improved signal-to-noise ratio and superresolution. 2015. ZEISS Technology Note

POSTER

Bringing Biology into Focus

THE PAST, PRESENT, AND FUTURE OF CONFOCAL MICROSOCOPY

Researchers and microscope makers alike are constantly striving to push the boundaries of sensitivity, resolution, and speed. Their determination has produced a steady stream of advances in microscope technology, and researchers armed with these ever-improving tools and techniques are squeezing ever more and better data out of their samples. This poster leads the reader through the past, present, and future of confocal microscopy. Additionally, you can go online to find an interactive version of the poster with additional information and graphics.

Go to poster.sciencemag.org/confocal

This poster is brought to you by the *Science*/AAAS Custom Publishing Office.

Finding answers in demanding research.

ZEISS LSM 800

Your compact confocal for high-end imaging

With ZEISS LSM 800 you are choosing a flexible and compact confocal laser scanning microscope, complete with highly sensitive GaAsP detector technology and fast linear scanning. Add Airyscan, the revolutionary detection concept from ZEISS, and you will gain 1.7× higher resolution in all three dimensions – resulting in a 5× smaller confocal volume. And you will be pushing sensitivity beyond the limits of all conventional confocals.

www.zeiss.com/lsm800

ZEISS